THESIS FOR THE DEGREE OF DOCTOR OF PHILOSOPHY

Voronoi Constellations for Coherent Fiber-Optic Communication Systems

Shen Li

CHALMERS
UNIVERSITY OF TECHNOLOGY

Communication Systems Group
Department of Electrical Engineering
Chalmers University of Technology
Gothenburg, Sweden, 2023

Voronoi Constellations for Coherent Fiber-Optic Communication Systems

Shen Li

ISBN 978-91-7905-879-1
Doktorsavhandlingar vid Chalmers tekniska högskola
Ny series nr 5345
ISSN 0346-718X

This thesis has been prepared using LaTeX and Tikz.

Communication Systems Group
Department of Electrical Engineering
Chalmers University of Technology
SE-412 96 Gothenburg, Sweden
Phone: +46 (0)31 772 1000
www.chalmers.se

Front cover illustration: A two-dimensional projection of the received 24-dimensional Voronoi constellation Λ_{24}^{72} (defined in [Paper D, Table 3]) at the same (uncoded) spectral efficiency as 64-ary quadrature amplitude modulation format after transmission over the additive white Gaussian noise channel.

Printed by Chalmers Reproservice
Gothenburg, Sweden, August 2023

Voronoi Constellations for Coherent Fiber-Optic Communication Systems

Shen Li
Communication Systems Group
Department of Electrical Engineering
Chalmers University of Technology

Abstract

The increasing demand for higher data rates is driving the adoption of high-spectral-efficiency (SE) transmission in communication systems. The well-known 1.53 dB gap between Shannon's capacity and the mutual information (MI) of uniform quadrature amplitude modulation (QAM) formats indicates the importance of power efficiency, particularly in high-SE transmission scenarios, such as fiber-optic communication systems and wireless backhaul links. Shaping techniques are the only way to close this gap, by adapting the uniform input distribution to the capacity-achieving distribution. The two categories of shaping are probabilistic shaping (PS) and geometric shaping (GS). Various methods have been proposed for performing PS and GS, each with distinct implementation complexity and performance characteristics. In general, the complexity of these methods grows dramatically with the SE and number of dimensions.

Among different methods, multidimensional Voronoi constellations (VCs) provide a good trade-off between high shaping gains and low-complexity encoding/decoding algorithms due to their nice geometric structures. However, VCs with high shaping gains are usually very large and the huge cardinality makes system analysis and design cumbersome, which motives this thesis.

In this thesis, we develop a set of methods to make VCs applicable to communication systems with a low complexity. The encoding and decoding, labeling, and coded modulation schemes of VCs are investigated. Various system performance metrics including uncoded/coded bit error rate, MI, and generalized mutual information (GMI) are studied and compared with QAM formats for both the additive white Gaussian noise channel and nonlinear fiber channels. We show that the proposed methods preserve high shaping gains of VCs, enabling significant improvements on system performance for high-SE transmission in both the additive white Gaussian noise channel and nonlinear fiber channel. In addition, we propose general algorithms for estimating the MI and GMI, and approximating the log-likelihood ratios in soft-decision forward error correction codes for very large constellations.

Keywords: Achievable information rates, coded modulation, coherent fiber-optic communications, constellation shaping, forward error correction coding, geometric shaping, lattices, multidimensional modulation formats, Voronoi constellations.

List of Publications

This thesis is based on the following publications:

[A] **S. Li**, A. Mirani, M. Karlsson, and E. Agrell, "Designing Voronoi constellations to minimize bit error rate," in *Proc. IEEE International Symposium on Information Theory (ISIT)*, Melbourne, Australia, July 2021.

[B] **S. Li**, A. Mirani, M. Karlsson, and E. Agrell, "Low-complexity Voronoi shaping for the Gaussian channel," *IEEE Transactions on Communications*, vol. 70, no. 2, pp. 865–873, 2022.

[C] **S. Li**, A. Mirani, M. Karlsson, and E. Agrell, "Power-efficient Voronoi constellations for fiber-optic communication systems," *Journal of Lightwave Technology*, vol. 41, no. 5, pp. 1298–1308, 2023.

[D] **S. Li**, A. Mirani, M. Karlsson, and E. Agrell, "Coded modulation schemes for Voronoi constellations," submitted to *IEEE Transactions on Communications*, 2023.

Other publications by the author not included in the thesis:

[E] **S. Li**, M. Karlsson, and E. Agrell, "Antialiased transmitter-side digital backpropagation," *IEEE Photonics Technology Letters*, vol. 32, no. 18, pp. 1211-1214, 2020.

[F] **S. Li**, M. Karlsson, and E. Agrell, "Improved simulation accuracy of the split-step Fourier method," in *Proc. Optical Fiber Communication Conference (OFC)*, San Diego, USA, March 2020.

[G] **S. Li**, C. Häger, N. Garcia, and H. Wymeersch, "Achievable information rates for nonlinear fiber communication via end-to-end autoencoder learning," in *Proc. European Conference on Optical Communication (ECOC)*, Rome, Italy, Sept. 2018.

[H] B. Chen, Z. Liang, **S. Li**, Y. Lei, G. Liga, and A. Alvarado, "On the performance of multidimensional constellation shaping for linear and nonlinear optical fiber channel," in *Proc. European Conference on Optical Communication (ECOC)*, Glasgow, Scotland, Sept. 2023. **(Invited paper)**

[I] A. Mirani, K. Vijayan, **S. Li**, Z. He, E. Agrell, J. Schröder, P. Andrekson, and M. Karlsson, "Physical realizations of multidimensional Voronoi constellations," *Journal of Lightwave Technology*, Early Access, 2023, doi: 10.1109/JLT.2023.3264927.

[J] A. Mirani, K. Vijayan, Z. He, **S. Li**, E. Agrell, J. Schröder, P. Andrekson, and M. Karlsson, "Comparison of physical realizations of multidimensional Voronoi constellations in single mode fibers," in *Proc. European Conference on Optical Communication (ECOC)*, Basel, Switzerland, Sept. 2022.

[K] A. Mirani, K. Vijayan, Z. He, **S. Li**, E. Agrell, J. Schröder, P. Andrekson, and M. Karlsson, "Experimental demonstration of 8-dimensional Voronoi constellations with 65,536 and 16,777,216 symbols," in *Proc. European Conference on Optical Communication (ECOC)*, Bordeaux, France, Sept. 2021.

Acknowledgements

First and foremost, I would like to express my deepest gratitude to my main supervisor, Prof. Erik Agrell, for your strong support, valuable guidance, and continuous encouragement during my Ph.D. journey. Apart from your great knowledge of lattice theory and fiber communications, I have always been impressed by your consistently meticulous attitudes and high standards on research, writing, and teaching, as well as your wisdom in life. You have been and will always be a great role model in my career and life. I am also grateful to my co-supervisor, Prof. Magnus Karlsson, who is an amiable and humorous gentleman and has been teaching me his insightful knowledge of fiber-optic communications. Having you as my supervisors is one of the luckiest things in my life. Special thanks go to my collaborators and friends, Dr. Ali Mirani, Zonglong He, and Ekaterina Deriushkina, for all the interesting discussions on Voronoi constellations and all the experimental knowledge you have taught me in the lab. I also wish to thank Prof. Bin Chen, for our collaborations on geometric shaping and the invitation of my research visit.

I would like to thank the head of our division, Prof. Erik Ström, and the head of the Communication Systems group, Prof. Fredrik Brännström, for creating and maintaining such a supportive work environment. Thanks the administrators at Electrical Engineering, Daniela and Natasha, for providing administrative support. Thanks Prof. Tommy Svensson, Prof. Alexandre Graell i Amat, and Mohammad Farsi for our good collaboration experience on teaching tasks. Thank you, Prof. Henk Wymeersch and Prof. Christian Häger, for introducing me to the world of research when I was a master's student.

There are some people who helped me with fiber simulation in the very beginning of my Ph.D., when I almost knew nothing. Thank you, Dr. Kamran Keykhosravi and Dr. Li Yan, for answering my naive questions with kindness and patience. I also acknowledge all colleagues in the FORCE group for nice seminars and presentations. I thank my colleagues and friends Hao, Roman, Chouaib, Chao, Han, and Ping, for sharing your knowledge with me. Thank you my previous office mates, Mohammad, Yibo, Yu, and Hyowon, for our cozy office vibe every day. I would like to thank all previous and current colleagues in the Communication Systems group for our friendly corridors and all the good time we have spent together. I wish everyone a bright career future.

I would also like to thank my friends outside Chalmers for always being there when I need them. Thank you Yanni, Guangan, Li, Mikael, Jiahui, Taoran, and Pin for all your support and our valuable friendship.

Last but not least, I want to take this chance to express my love to my parents, grandparents, and my fiancé Haoge and his family. You are everything to me.

Shen Li
Gothenburg, July, 2023

Financial Support

This work was funded by the Swedish Research Council (VR) under grants no. 2017-03702 and no. 2021-03709, and the Knut and Alice Wallenberg (KAW) Foundation under grant no. 2018.0090. Part of the simulations were performed on the resources provided by the Swedish National Infrastructure for Computing (SNIC) at C3SE.

Acronyms

1D	one-dimensional
2D	two-dimensional
4D	four-dimensional
8D	eight-dimensional
AIR	achievable information rate
APE	asymptotic power efficiency
ASE	amplified spontaneous emission
AWGN	additive white Gaussian noise
B2B	back-to-back
BER	bit error rate
BICM	bit-interleaved coded modulation
BRGC	binary reflected Gray code
CD	chromatic dispersion
CLPQ	closest lattice point quantizer
CM	coded modulation
DBP	digital backpropagation
DSP	digital signal processing
FFT	fast Fourier transform
FEC	forward error correction
GMI	generalized mutual information
GN	Gaussian noise

GS	geometric shaping
HD	hard-decision
LDPC	low-density parity-check code
LUT	look-up table
IFFT	inverse fast Fourier transform
I/Q	in-phase and quadrature
LLR	log-likelihood ratio
MAP	maximum a posteriori
MD	mutidimensional
MED	minimum Euclidean distance
ML	maximum likelihood
MLCM	multilevel coded modulation
MI	mutual information
MSD	multistage decoding
nD	n-dimensional
NLI	nonlinear interference
NNA	nearest neighbor approximation
OSNR	optical signal-to-noise ratio
PAM	pulse amplitude modulation
PAPR	peak-toaverage power ratio
PS	probabilistic shaping
QAM	quadrature amplitude modulation
SD	soft-decision

SE	sepctral efficiency
SER	symbol error rate
SNR	signal-to-noise ratio
SP	set partitioning
SSFM	split-step Fourier method
VC	Voronoi constellation
WDM	wavelength-division multiplexing

Contents

Part I

Overview

CHAPTER 1

Introduction

Driven by emerging technologies such as the Internet of Things, cloud computing, virtual meetings, video conferencing, etc., the demand for higher data rates and spectral efficiencies (SEs) in wireless and wired communication systems continues to increase. For example, in the past two decades, the data rate of coherent optical systems has evolved from 40/100 Gbps [1–3] to 200 Gbps [4], then to 400 Gbps [5] and 800 Gbps [6] per wavelength recently.

The high demand for SE implies a trend towards high-order modulation formats, such as the commonly deployed 64-ary and 256-ary quadrature amplitude modulation (QAM) formats in the fifth generation wireless communication networks [7, 8] and high-throughput fiber-optic experiments [9–11]. Together with higher-order modulation formats, larger baud rates, powerful soft-decision (SD) forward error correction (FEC) codes, and high-performance digital signal processing (DSP) are the key enablers of high throughput data links.

In general, power efficiency becomes important for high-SE modulation formats, as the gap between Shannon's capacity and the achievable information rates (AIRs) with equally probable QAM[1] formats increases with the SE (will be explained in section 3.3). An important technique, called signal shaping, aiming at adapting the input distribution to the capacity-achieving distribution to close this gap, has been intensively studied in both the wireless [12–14] and optical communities [11, 15–21], and deployed in today's commercial products [6, 22, 23].

There are two categories of constellation shaping: probabilistic shaping (PS) [15–19,24]

[1] Throughout this thesis, "QAM" refers to two-dimensional (2D) square and cross QAM if not otherwise specified.

and geometric shaping (GS) [11,20,21,25–29], where the former changes the probabilities of symbols in a QAM constellation and the latter changes the position of equally probable symbols in a constellation. PS uses a distribution matcher [30] to map information bits to transmitted symbols with a desired distribution, e.g., a Maxwell–Boltzmann distribution. A popular way of performing GS at high SEs is using gradient descent algorithms to optimize the mutual information (MI) or generalized mutual information (GMI), usually resulting in irregular constellations that require look-up tables (LUTs) to encode and decode. Comparing the complexity of these two methods is cumbersome, as their implementation ways are very different. One sure thing is that the complexity of both the distribution matcher in PS and the LUT in GS increases dramatically at high SEs. There have been results showing that one-dimensional (1D) and 2D geometrically shaped constellations with a small cardinality are suboptimal compared with PS [31]. However, better performance is expected for GS in multidimensional (MD) cases with large constellation cardinalities. All of these motivate the need for designing low-complexity regular geometrically shaped constellations, to achieve comparable shaping gains with a lower complexity than current PS and GS methods, and be able to work at high SEs when other methods break down due to complexity constraints.

Voronoi constellations (VCs), proposed by Conway and Sloane in 1983 [32] and then generalized by Forney in 1989 [33] are a structured GS method with high shaping gains and a good potential to solve the aforementioned issues. As their encoding and decoding do not need LUTs, the complexity does not increase with the SE [32,34]. In particular, a set of methods called "shaping for lattice codes" [35–37], in which lattice codes are used as FEC codes, jointly designs shaping and FEC and has the potential of achieving Shannon's capacity [38,39]. The symbol error rate (SER) and bit error rate (BER) have been studied for the additive white Gaussian noise (AWGN) channel [13,40–43]. In this thesis, we propose our VCs in a different manner, where shaping and FEC coding are separated, which allows for independent study of the MI, GMI, and labeling of VCs, and independent use of arbitrary FEC codes. The designed VCs show good gains over QAM in terms of uncoded BER, MI, and GMI for both the linear Gaussian channel (papers A and B) and nonlinear fiber channels (paper C). High coded BER gains over QAM are found for the Gaussian channel in paper D. We conjecture the effectiveness of using the designed VCs for shaping for other channels as well, such as wireless fading channels, etc.

1.1 Thesis organization

This thesis consists of two parts, where the goal of Part I is to provide necessary background knowledge to help understand the appended papers in Part II. The published or submitted papers in Part II focus on designing a set of methods to apply VCs for both the linear AWGN channel and nonlinear fiber-optic channels. Thus, the rest of Part I is organized as follows. Chapter 2 introduces the system models, including the AWGN channel and fiber-optic communication systems. In Chapter 3, the definition and the

parameters used for designing and comparing modulation formats are described. The motivation behind performing GS is explained, and several typical coded modulation (CM) schemes in fiber-optic communication systems are introduced. Chapter 4 discusses the design of the proposed VCs, including parameters selection, encoding/decoding algorithms, labeling algorithms, CM schemes, and the estimation of AIRs for VCs. Chapter 5 summarizes the contributions of the appended papers, providing an overview of the flow and relationship among these papers.

1.2 Notation

Bold lowercase symbols denote row vectors and bold uppercase symbols denote random vectors or matrices. The elements of a vector $\boldsymbol{u}$ are denoted by u_i, the rows of a matrix $\boldsymbol{P}$ are denoted by $\boldsymbol{p}_i$, and the element at row i, column j of a matrix $\boldsymbol{P}$ are denoted by P_{ij}. The sets of integer, real, and natural numbers are denoted by $\mathbb{Z}$, $\mathbb{R}$, and $\mathbb{N}$, respectively. Other sets are denoted by calligraphic symbols. Rounding a vector to its nearest integer vector is denoted by $\lfloor \cdot \rceil$, in which ties are broken arbitrarily. The largest integer not greater than a given real number is denoted by $\lfloor \cdot \rfloor$. The cardinality of a set or the order of a lattice partition is denoted by $|\cdot|$.

CHAPTER 2

System Model

In this chapter, we introduce the system model considered in this thesis and describe the two considered channels: the AWGN channel and the fiber-optic channel.

2.1 Block diagram

Fig. 2.1 depicts a simplified communication system. The overall goal is to reliably transmit information bits from one end to the other. The FEC encoder adds redundancy to protect these information bits, at the cost of a loss in information rate. The encoded bit stream is parallelized and then every block of bits $\boldsymbol{b}$ is mapped to an MD symbol $\boldsymbol{x}$ according to a modulation format $\mathcal{X}$, also known as constellation. The symbols are

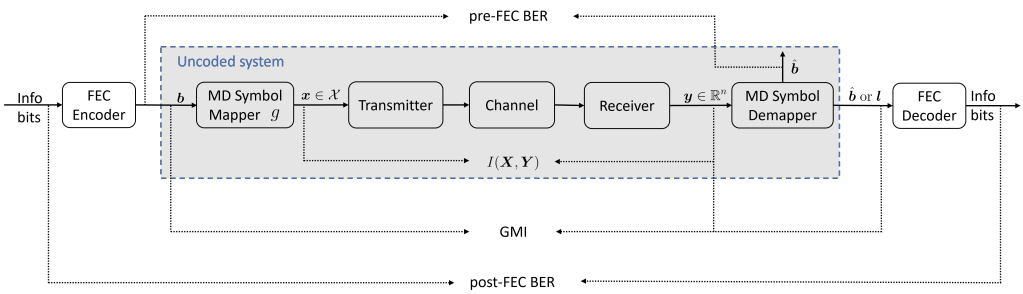

Figure 2.1: Block diagram of a simplified communication system.

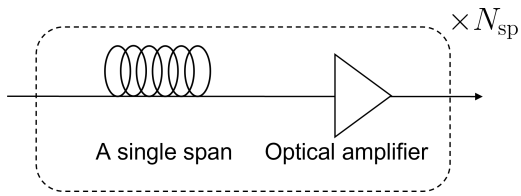

Figure 2.2: A fiber link with N_{sp} spans.

imposed onto an analog eletrical or optical signal and transmitted by the transmitter over the channel. After receiving the distorted signal, DSP techniques in the receiver compensate channel impairments and the receiver outputs a noisy version of the transmitted symbol $\boldsymbol{y}$. The input to the MD symbol demapper is considered memoryless. Then, log-likelihood ratios (LLRs) $\boldsymbol{l}$ are calculated or $\hat{\boldsymbol{b}}$ are mapped back according to a detecting rule by the MD symbol demapper, depending on SD or hard-decision (HD) decoding. Finally, the FEC decoder recovers the information bits back.

Let $\boldsymbol{X}$ and $\boldsymbol{Y}$ denote the nD random vectors representing the transmitted and received symbols (after the symbol mapper and before the symbol demapper), respectively. An important channel model is the AWGN model,

$$\boldsymbol{Y} = \boldsymbol{X} + \sigma \boldsymbol{Z}, \tag{2.1}$$

where the random vector $\boldsymbol{Z} \sim \mathcal{N}(\boldsymbol{0}, \boldsymbol{I}_n)$ with $\boldsymbol{0}$ being the all-zero vector and $\boldsymbol{I}_n$ being the $n \times n$ identity matrix.

The AWGN channel is reliable to model many satellite and deep space communication links. It is also accurate for modeling the back-to-back (B2B) case in optical communications. Except for the white Gaussian noise, this model does not consider other phenomena occurring in wireless or wired channels, such as fading, dispersion, nonlinearity, channel memory, etc. However, analyzing system performance for these scenarios assuming the AWGN channel still provides insights for system design. Moreover, its simplicity and traceability allow for deriving theoretical performance limits. For example, the SER and BER can be exactly calculated or well approximated under some conditions.

2.2 Fiber-optic channels

This section first introduces the signal propagation along the optical channel, then introduces three commonly used channel models when designing algorithms for fiber-optic communication systems.

2.2.1 Signal Propagation in the Fiber-Optic Channel

Fig. 2.2 illustrates a fiber link that is divided into N spans of single-mode fiber, which belongs to the "Channel" block in Fig. 2.1. Each span has a typical length L ranging

from 50 to 120 km, depending on the application. The purpose of dividing the link into spans is to periodically add an optical amplifier to boost the signal power in each span.

The signal evolution in a single polarization along the fiber is generally governed by the scalar nonlinear Schrödinger equation

$$\frac{\partial E(t,z)}{\partial z} = \underbrace{-\frac{\alpha}{2}E(t,z)}_{\text{Attenuation}} \underbrace{-j\frac{\beta_2}{2}\frac{\partial^2 E(t,z)}{\partial t^2}}_{\text{Dispersion}} + \underbrace{j\gamma\left|E(t,z)\right|^2 E(t,z)}_{\text{Nonlinearity}}, \tag{2.2}$$

where $E(t,z)$ is the electrical field in complex baseband propagation along the fiber at time t and distance z, α is the attenuation factor, β_2 is the group velocity dispersion parameter, and γ is the nonlinear parameter. Optical light has two orthogonal polarizations, the x and y polarization. Let $\boldsymbol{E}(t,z) = [E_x(t,z)\ E_y(t,z)]^{\mathrm{T}}$ be the electrical field of the two polarizations. Then the dual-polarization signal propagation in an unamplified fiber span (before the optical amplifier) can be modeled by the Manakov equation [44]

$$\frac{\partial \boldsymbol{E}(t,z)}{\partial z} = \underbrace{-\frac{\alpha}{2}\boldsymbol{E}(t,z)}_{\text{Attenuation}} \underbrace{-j\frac{\beta_2}{2}\frac{\partial^2 \boldsymbol{E}(t,z)}{\partial t^2}|}_{\text{Dispersion}} + \underbrace{j\frac{8}{9}\gamma\left\|\boldsymbol{E}(t,z)\right\|^2 \boldsymbol{E}(t,z)}_{\text{Nonlinearity}}, \tag{2.3}$$

where the coefficient 8/9 is the result of averaging over the rapidly changing polarization states.

The nonlinear Schrödinger equation and Manakov equation describe the three main impairments along the fiber: the fiber loss, chromatic dispersion (CD), and nonlinear Kerr effects. However, it is a time-dependent nonlinear differential partial equation which cannot be solved analytically. In the following, we will explain the effect of each impairment separately by neglecting other terms in (2.3).

Fiber loss and amplifier noise

If we only consider the attenuation and neglect the dispersion and nonlinearity, a closed-form solution is found

$$\boldsymbol{E}(t,z) = \boldsymbol{E}(t,0)\exp\left(-\alpha z/2\right). \tag{2.4}$$

As can be seen, the electrical field degrades with the distance z as $\exp(-\alpha z/2)$. The signal power $P(z)$ at distance z attenuates as

$$P(z) = P(0)\exp\left(-\alpha z\right). \tag{2.5}$$

The attenuation factor α determines the power loss and is typically expressed in decibels per km, i.e.,

$$\begin{aligned}\alpha_{\mathrm{dB}} &= -\frac{10}{z}\log_{10}\left(\frac{P(z)}{P(0)}\right)\ [\mathrm{dB/km}] \\ &= (10\log_{10} e)\alpha.\end{aligned} \tag{2.6}$$

This power loss is usually compensated by an optical amplifier (except for unamplified links). Most systems insert an erbium-doped fiber amplifier at the end of each span. The power gain of the amplifier is $G = \exp(\alpha L)$, which fully compensates the loss in the span. However, the amplifier also introduces amplified spontaneous emission (ASE) noise, which can be modeled as a Gaussian-distributed random noise, with a power of

$$P_{\mathrm{ASE}} = \frac{1}{2} F_{\mathrm{n}} h\nu (G-1) R_{\mathrm{s}} \tag{2.7}$$

for a single polarization, where F_{n} is the amplifier noise figure, h is the Planck constant, and ν is the carrier frequency. The signal-to-noise ratio (SNR) after N amplifiers is defined as

$$\mathrm{SNR} = \frac{P_{\mathrm{ch}}}{N P_{\mathrm{ASE}}}, \tag{2.8}$$

where P_{ch} is the transmitted signal power of a single polarization. The accumulation of the ASE noise power leads to a degradation in SNR after each fiber span.

Chromatic dispersion

Setting $\alpha = \gamma = 0$ in (2.3) gives the closed-form solution

$$\boldsymbol{E}(\omega, z) = \boldsymbol{E}(\omega, 0) \exp(j\omega^2 \beta_2 z/2), \tag{2.9}$$

where $\boldsymbol{E}(\omega, z)$ represents the electrical field in the frequency domain at angular frequency ω and distance z. The spectrum of the transmitted signal is distorted by an all-pass filter $H(\omega) = \exp(j\omega^2 \beta_2 z/2)$, and different frequency components experience different distortions. The phenomenon is called CD, due to that different frequency components of a light travel in the fiber at different speeds. The frequency-dependent phase shift caused by $H(\omega)$ results in pulse broadening in the time domain. The extent of the time-domain broadening ΔT after transmission over a single-mode fiber for a distance z is

$$\Delta T = \beta_2 z \Delta\omega, \tag{2.10}$$

where β_2 has the unit of [ps^2/km]. Usually another quantity, called the *dispersion parameter*

$$D = -\frac{2\pi c}{\lambda^2} \beta_2 \ [\mathrm{ps/km \cdot nm}] \tag{2.11}$$

is used to describe CD, where c is the speed of light and λ is the wavelength of the light. For a standard single-mode fiber, $D \approx 17$ ps/(km $\cdot$ nm) at $\lambda = 1550$ nm.

CD can be compensated in the optical domain by concatenating a dispersion-compensation fiber with $D < 0$, or it can be equalized in the electrical domain by time-domain or frequency-domain digital finite impulse response or infinite impulse response filters [45, 46]. The compensation idea is based on the inverse frequency response

$$H^{-1}(\omega) = \exp(-j\omega^2 \beta_2 z/2). \tag{2.12}$$

Nonlinear Kerr effect

The refractive index of the fiber increases with the intensity of optical light, a phenomenon known as the nonlinear Kerr effect. Since the nonlinearity is dependent on the signal power, we consider only the attenuation term and neglect the dispersion in (2.3). This simplification leads to a closed-form solution

$$\boldsymbol{E}(t,z) = \boldsymbol{E}(t,0)\exp(-\alpha z/2)\exp\left(j\frac{8}{9}\gamma\|\boldsymbol{E}(t,0)\|^2 L_{\text{eff}}(z)\right), \tag{2.13}$$

where

$$L_{\text{eff}}(z) = \int_0^z e^{-\alpha x}\mathrm{d}x = \frac{1-e^{-\alpha z}}{\alpha} \tag{2.14}$$

is called the effective length. From (2.13), we can observe that the Kerr effect in the absence of dispersion only causes a power-dependent phase shift in the time domain, which results in spectral broadening in the frequency domain.

2.2.2 Channel models

Without a closed-form solution, numerical and analytical models exist to capture full or partial characteristics of the Manakov equation. This section introduces two commonly used channel models for fiber-optic communication systems, the SSFM and the GN model. Furthermore, we explain the reason why the linear AWGN model is also widely used in the fiber-optic community.

Split-step Fourier method

The split-step Fourier method (SSFM) is an accurate numerical way of simulating the Manakov equation, and usually served as a reference model for simulation and validation. The idea is to discretize the signal propagation along each span of fiber into K small spatial steps, such that the nonlinearity and dispersion can be separated and expressed analytically in each step.

Let $\Delta z = L/K$ be the step size, $\hat{N} = \exp(j\frac{8}{9}\gamma\Delta z\|\boldsymbol{E}\|^2)$ be the nonlinearity operator that depends on the power of its input signal $\boldsymbol{E}$, $\hat{D} = \exp(j\omega^2\beta_2\Delta z/2)$ be the dispersion operator, and $\hat{L} = \exp(-\alpha\Delta z/2)$ be the loss operator. Fig. 2.3 illustrates the structure of the SSFM for a single fiber span. In each small step, the nonlinearity, dispersion, and the loss operator are performed successively. The transforms of the electrical field between the time domain and frequency domain are performed using the fast Fourier transform (FFT) and inverse fast Fourier transform (IFFT). After K steps, the signal is amplified and the ASE noise is added.

The accuracy of SSFM has been widely studied in the literature. In general, the step size Δz needs to be sufficiently small for the output of the SSFM to converge. Moreover, high oversampling rates are required to capture the spectral broadening of

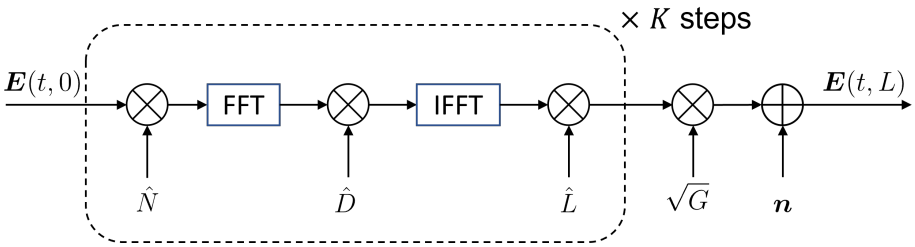

Figure 2.3: The SSFM structure of signal transmitted in one fiber span with K steps.

signal propagation [47, 48]. These indicate a trade-off between the simulation accuracy and complexity. Various refinements have been proposed for SSFM, including optimizing the selection and updating rules of the step size [49–53], using low-pass filters to filter the linear steps [54], implementing the dispersion operator in the time domain [55], etc.

The SSFM can also be used as an effective technique for compensating the linear and nonlinear impairments in fiber transmission. This is achieved by solving (2.3) with opposite signs of all terms, a method known as digital backpropagation (DBP). DBP can be implemented at the transmitter side before signal transmission [56, 57], at the receiver side [3, 58], or at both sides [59]. Due to complexity limitations, DBP uses a much larger step size and a lower oversampling rate compared to the forward SSFM used for simulating signal propagation. Various methods have been proposed to reduce the complexity of DBP [58, 60–62]. Note that DBP cannot perfectly recover the transmitted signal even with an exact reverse of the forward SSFM, due to the interaction between signal and noise. To address this, stochastic DBP [63] has been introduced, which takes into account the statistics of the amplifier noise, thereby improving the performance of standard DBP.

The Gaussian noise model

Although the SSFM is sufficiently accurate, such numerical methods generally have a high computation complexity and are not analytically friendly. Therefore, it is important to have simpler models that can capture the main characteristics of the fiber channel while being more computationally efficient. The Gaussian noise (GN) model is one such simpler model that can predict system performance much faster than the SSFM, and sufficiently reliable under some conditions. The motivation behind the GN model is that in a dispersed link, the nonlinear interference (NLI) is relatively small and can be treated as additive Gaussian noise.

The GN model with transmitted 2D (complex) symbols $\boldsymbol{X}$ and received complex symbols $\boldsymbol{Y}$ is expressed as

$$\boldsymbol{Y} = \boldsymbol{X} + \sqrt{P_{\mathrm{ASE}} + P_{\mathrm{NLI}}}\boldsymbol{Z}, \tag{2.15}$$

where $\boldsymbol{Z} \sim \mathcal{N}(\boldsymbol{0}, \boldsymbol{I}_2)$ with $\boldsymbol{0}$ being the all-zero vector and $\boldsymbol{I}_2$ being the 2×2 identity matrix, P_{NLI} is the NLI noise power, and

$$P_{\mathrm{ASE}} = F_{\mathrm{n}} h\nu (G-1) R_{\mathrm{s}} \tag{2.16}$$

is the ASE noise power with R_{s} being the symbol rate. The expression of P_{NLI} depends on a variety of system parameters, which is well studied and derived in the literature [64]. For example, suppose the following assumptions:

- Dual-polarization transmission.
- Every span contains the same fiber type with the same length.
- Lumped amplification.
- The loss of each fiber span is fully compensated by the amplifier.
- All wavelength-division multiplexing (WDM) channels are identical, i.e, they have the same channel spacing Δf, symbol rate, launch power per channel P_{ch}, and transmit the same modulation format.
- The number of WDM channels N_{ch} is odd.
- The power spectral density of the NLI noise is flat over R_{s}.

Under these conditions, the NLI power of the center channel is approximated as [64, Eq. (16), (26), (39)]

$$P_{\mathrm{NLI}} = N^{1+\epsilon} \frac{8\gamma^2 L_{\mathrm{eff}}^2(L) P_{\mathrm{ch}}^3 \alpha}{27\pi |\beta_2| R_{\mathrm{s}}^2} \operatorname{arcsinh}\left(\frac{\pi^2 |\beta_2| R_{\mathrm{s}}^2 N_{\mathrm{ch}}^{2R_{\mathrm{s}}/\Delta f}}{2\alpha} \right), \tag{2.17}$$

where arcsinh is the inverse hyperbolic sine function and

$$\epsilon \approx \frac{3}{10} \log_e \left(1 + \frac{6}{L\alpha \operatorname{arcsinh}\left(\frac{\pi^2 |\beta_2| R_{\mathrm{s}}^2 N_{\mathrm{ch}}^{2R_{\mathrm{s}}/\Delta f}}{2\alpha} \right)} \right). \tag{2.18}$$

The GN model serves as a conservative (as it overestimates the NLI power) and convenient tool for predicting system performance. Its prediction accuracy depends on system parameters and has been extensively validated through both SSFM simulation and experiments [64–66]. Actually, the NLI noise is not additive Gaussian but depends on the transmitted modulation format [67]. Thus, the enhanced GN model [68] was proposed which takes into account the dependency of the NLI power on different modulation formats.

The additive white Gaussian noise model

An even simpler model than the GN model is the AWGN model introduced in section 2.1. The AWGN model is equivalent to the widely used B2B scenario in fiber-optic communication systems, where no fiber is present but only the optical amplifier is considered. In the B2B case, the commonly used metric is the optical signal-to-noise ratio (OSNR), measured as

$$\mathrm{OSNR} = \frac{\mathrm{SNR} \cdot R_\mathrm{s}}{B_n} \tag{2.19}$$

where B_n is typically set to 12.5 GHz, corresponding to the 0.1 nm resolution bandwidth of an optical signal analyzer.

Apart from the B2B scenario, the AWGN model is also reliable when the amplifier noise is dominant over other impairments or when other impairments are well compensated by DSP. Comparing the performance of different modulation formats or DSP algorithms under the same AWGN channel is fair and fast, and the performance gain implies better tolerance to amplifier noise, which can increase the system's reach. Thus, the AWGN channel is a very popular model when designing algorithms for fiber-optic communication systems.

CHAPTER 3

Coded Modulation

In Fig. 2.1, the joint design of the symbol mapper/demapper (including the modulation format $\mathcal{X}$ and labeling function g) and FEC encoder/decoder is called a CM scheme. This chapter first introduces the definition and important figures of merit of a modulation format, then discusses GS and introduces some typical CM schemes.

3.1 Modulation formats

A modulation format, or a constellation, represents a codebook that specifies how bits are modulated onto carriers. Modulation formats is a key aspect that directly affects the data rate in communication systems.

An n-dimensional (nD) *constellation* is an alphabet $\mathcal{X} = \{\boldsymbol{x}_1, \boldsymbol{x}_2, \ldots, \boldsymbol{x}_M\}$, containing M nD real vectors with a probability mass function $p_{\boldsymbol{X}}(\boldsymbol{x})$. The average symbol energy is

$$E_{\mathrm{s}} = \sum_{\boldsymbol{x}\in\mathcal{X}} p_{\boldsymbol{X}}(\boldsymbol{x})\|\boldsymbol{x}\|^2. \tag{3.1}$$

The MD symbol is usually assigned to the following orthogonal physical dimensions: the in-phase and quadrature (I/Q) pairs, polarizations, time slots, frequencies/wavelengths, and spatial dimensions, such as multiple antennas in wireless communications and multicore/multimode fibers in optical communications. For example, Fig. 3.1 illustrates the dimension realization of coherent optical communication systems. Different physical dimension realizations might result in different system performance, and involve

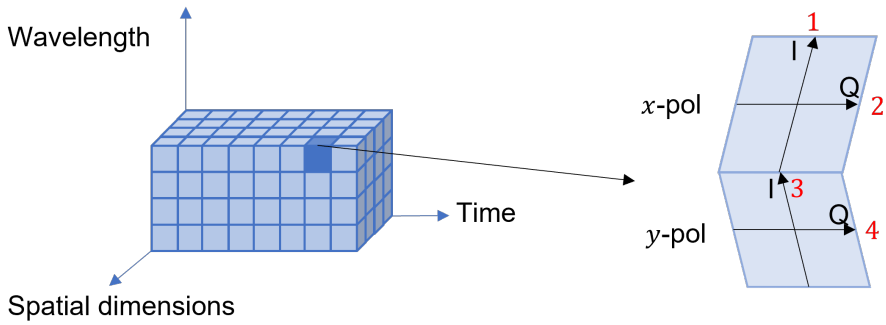

Figure 3.1: Physical dimension realization of MD constellations in fiber-optic communication systems. Each three-dimensional cube on the left represents a four-dimensional (4D) symbol on the right, containing two I/Q pairs in two orthogonal polarizations x and y.

different transmitter/receiver setup and DSP algorithms, thereby introducing different complexity.

Each MD symbol $\boldsymbol{x}$ carries $m = \log_2(M)$ bits $\boldsymbol{b} = (b_1, \ldots, b_m)$. The bit-to-symbol mapping function g from $\boldsymbol{b}$ to $\boldsymbol{x}$ carried out in the MD symbol mapper in Fig. 2.1 is called *constellation labeling*

$$g: \{0,1\}^m \to \mathcal{X}. \tag{3.2}$$

Let the random vector $(B_1, \ldots, B_m)$ represent the labels of the transmitted random symbol $\boldsymbol{X}$.

3.2 Performance metrics

This section introduces useful performance metrics to evaluate different modulation formats.

3.2.1 Spectral efficiency

The (uncoded) *spectral efficiency* [29, 69, 70] is usually normalized per two dimensions, i.e., per I/Q pair, defined as

$$\beta = \frac{2m}{n} \text{ [bits/2D-symbol]}. \tag{3.3}$$

The granularity of β is also important as it influences the flexibility of selecting data rates according to requirements. For the most commonly used 2D square or cross M-QAM formats where M is a power of 2, the granularity is 1 bit/2D-symbol.

Another commonly used definition of the SE of a data link is defined as

$$\beta_{\text{link}} = \frac{R_{\text{b}}}{B} \text{ [bits/s/Hz]}, \tag{3.4}$$

where R_{b} is the bit rate and B is the occupied frequency bandwidth. This quantity considers the physical implementation including the added guard band, pilot overhead, FEC overhead, and other overheads. When no such overheads are considered and Nyquist pulse shaping is used, $\beta_{\text{link}} = \beta$.

3.2.2 Uncoded symbol and bit error rate

The block diagram of an uncoded system is shown inside the dashed border in Fig. 2.1. The memoryless MD symbol demapper first estimates the transmitted symbol $\hat{\boldsymbol{x}}$ according to a detection rule, and then maps $\hat{\boldsymbol{x}}$ to its bit labels $\hat{\boldsymbol{b}} = (\hat{b}_1, \ldots, \hat{b}_m)$.

Upon receiving a symbol $\boldsymbol{y} \in \mathbb{R}^n$, which is a noisy version of $\boldsymbol{x}$, the optimal detection rule that minimizes the probability of detection error is the maximum a posteriori (MAP) detection rule

$$\hat{\boldsymbol{x}}_{\text{MAP}}(\boldsymbol{y}) = \underset{\boldsymbol{x}\in\mathcal{X}}{\arg\max}\, f_{\boldsymbol{Y}|\boldsymbol{X}}(\boldsymbol{x}|\boldsymbol{y}). \tag{3.5}$$

For equally probable transmitted symbols with $p_{\boldsymbol{X}}(\boldsymbol{x}) = 1/M$, the MAP rule is equivalent to the maximum likelihood (ML) rule

$$\hat{\boldsymbol{x}}_{\text{ML}}(\boldsymbol{y}) = \underset{\boldsymbol{x}\in\mathcal{X}}{\arg\max}\, f_{\boldsymbol{Y}|\boldsymbol{X}}(\boldsymbol{y}|\boldsymbol{x}), \tag{3.6}$$

where $f_{\boldsymbol{Y}|\boldsymbol{X}}(\boldsymbol{y}|\boldsymbol{x})$ is the channel transition probability density function.

For the AWGN channel,

$$f_{\boldsymbol{Y}|\boldsymbol{X}}(\boldsymbol{y}|\boldsymbol{x}) = \frac{1}{(2\pi\sigma^2/n)^{n/2}} \exp\left(-\frac{\|\boldsymbol{y}-\boldsymbol{x}\|^2}{2\sigma^2/n}\right), \tag{3.7}$$

where σ^2 is the total noise power for n real dimensions. Then the ML decoding rule is

$$\begin{aligned}\hat{\boldsymbol{x}}_{\text{ML,AWGN}}(\boldsymbol{y}) &= \underset{\boldsymbol{x}\in\mathcal{X}}{\arg\max}\, \frac{1}{(2\pi\sigma^2/n)^{n/2}} \exp\left(-\frac{\|\boldsymbol{y}-\boldsymbol{x}\|^2}{2\sigma^2/n}\right) \\ &= \underset{\boldsymbol{x}\in\mathcal{X}}{\arg\min}\, \|\boldsymbol{y}-\boldsymbol{x}\|^2 \end{aligned} \tag{3.8}$$

For the nonlinear fiber channel, $\boldsymbol{y}$ represents the memoryless symbol after DSP and $f_{\boldsymbol{Y}|\boldsymbol{X}}(\boldsymbol{y}|\boldsymbol{x})$ is not known analytically. Thus, mismatched decoding is performed, where $f(\boldsymbol{y}|\boldsymbol{x})$ is selected to be a Gaussian distribution. The decoding rule remains the same as in (3.8).

Transmitting a constellation $\mathcal{X}$, the uncoded SER measures the average probability of the decoder making an error, defined as

$$P_{\mathrm{s}} = \sum_{\boldsymbol{x}\in\mathcal{X}} p_{\boldsymbol{X}}(\boldsymbol{x})\Pr(\hat{\boldsymbol{x}} \neq \boldsymbol{x}|\boldsymbol{x}). \tag{3.9}$$

Let $d_{\mathrm{E}}(\boldsymbol{u},\boldsymbol{v})$ denote the Euclidean distance between two vectors $\boldsymbol{u}$ and $\boldsymbol{v}$, $d_{\min}$ denote the minimum Euclidean distance (MED) of the constellation, and $A_{\min}(\boldsymbol{x})$ denote the number of nearest neighbors of $\boldsymbol{x}$ at Euclidean distance $d_{\min}$ in a constellation $\mathcal{X}$, i.e.,

$$A_{\min}(\boldsymbol{x}) = |\{\tilde{\boldsymbol{x}} \in \mathcal{X} : d_{\mathrm{E}}(\boldsymbol{x},\tilde{\boldsymbol{x}}) = d_{\min}\}|. \tag{3.10}$$

For a constellation with equally likely symbols transmitted over the AWGN channel, the uncoded SER in (3.9) can be approximated by the nearest neighbor approximation (NNA)

$$P_{\mathrm{s}} \approx \underbrace{\frac{1}{M}\sum_{\boldsymbol{x}\in\mathcal{X}} A_{\min}(\boldsymbol{x})}_{\bar{A}_{\min}} \cdot \frac{1}{2}\operatorname{erfc}\left(\sqrt{\frac{d_{\min}^2}{4N_0}}\right), \tag{3.11}$$

where $\bar{A}_{\min}$ is the average number of nearest neighbors of the constellation, N_0 is the total noise variance, and $\operatorname{erfc}(\,\cdot\,)$ is the complementary error function. The NNA is asymptotically exact for high E_{s}/N_0.

The uncoded BER is defined as the average error probability over all bit positions, i.e.,

$$P_{\mathrm{b}} = \frac{1}{m}\sum_{k=1}^{m}\sum_{\boldsymbol{x}\in\mathcal{X}} p_{\boldsymbol{X}}(\boldsymbol{x})\Pr(\hat{b}_k \neq b_k|\boldsymbol{x}), \tag{3.12}$$

where $\hat{b}_k$ is the kth bit of $\hat{\boldsymbol{x}}$.

For a constellation with equally likely symbols transmitted over the AWGN channel, the NNA of the uncoded BER is

$$\begin{aligned} P_{\mathrm{b}} &\approx \frac{1}{m}\sum_{k=1}^{m}\frac{1}{M}\sum_{\boldsymbol{x}\in\mathcal{X}} A_{\min}^{k}(\boldsymbol{x})\Pr(d_{\mathrm{E}}(\hat{\boldsymbol{x}},\boldsymbol{x}) = d_{\min}|\boldsymbol{x}) \\ &= \frac{1}{m}\cdot\underbrace{\frac{1}{M}\sum_{\boldsymbol{x}\in\mathcal{X}}\sum_{k=1}^{m} A_{\min}^{k}(\boldsymbol{x})}_{G_{\mathrm{p}}}\cdot\frac{1}{2}\operatorname{erfc}\left(\sqrt{\frac{d_{\min}^2}{4N_0}}\right) \end{aligned} \tag{3.13}$$

where

$$A_{\min}^{k}(\boldsymbol{x}) = |\{\tilde{\boldsymbol{x}} \in \mathcal{X} : d_{\mathrm{E}}(\tilde{\boldsymbol{x}},\boldsymbol{x}) = d_{\min},\ \tilde{b}_k \neq b_k\}|, \tag{3.14}$$

and the bit labels of $\tilde{\boldsymbol{x}}$ are represented by $\tilde{\boldsymbol{b}} = (\tilde{b}_1, \ldots, \tilde{b}_m)$. The expression G_p refers to the average number of different bits per pair of adjacent symbols, which is known as the Gray penalty and will be discussed further in section 3.2.4.

Fiber-optic communication systems require the BER after FEC decoding, called the "post-FEC BER" (as shown in Fig. 2.1), to be lower than 10^{-15}. In practice, due to complexity limitations, a "pre-FEC" BER is often simulated before applying an HD FEC code. This pre-FEC BER is either the uncoded BER or the BER after decoding of the inner SD FEC codes if concatenated CM is used. The design criterion is usually to aim for a pre-FEC BER between 10^{-4} and 10^{-2}, and then the HD FEC code can further suppress the residual error down to 10^{-15}.

3.2.3 Asymptotic power efficiency

From (3.11), we can observe that the SER is related to the argument $\sqrt{\frac{d_\mathrm{min}^2}{4N_0}}$ inside the complementary error function. To measure how power-efficient a constellation at a given d_min, a parameter γ is defined satisfying

$$\begin{aligned} \gamma \frac{E_\mathrm{b}}{N_0} &= \frac{d_\mathrm{min}^2}{4N_0} \\ \Rightarrow \gamma &= \frac{d_\mathrm{min}^2}{4E_\mathrm{b}}, \end{aligned} \tag{3.15}$$

where $E_\mathrm{b} = E_\mathrm{s}/m$. The γ is called the *asymptotic power efficiency* (APE) [71, Eq. (5.8)], [29] of a constellation (with equally probable symbols). At high E_s/N_0, if two constellations have the same $\bar{A}_\mathrm{min}$, a constellation with a greater γ requires a smaller E_b/N_0 for a certain P_s, thus considered more power-efficient.

Pulse amplitude modulation (PAM) format (with $M = 2^\beta$ levels equally spaced symmetrically around the origin) has an APE of

$$\gamma_\mathrm{PAM} = \frac{3\beta}{2(2^\beta - 1)} \tag{3.16}$$

at SE β. An nD cubic constellation constructed by the Cartesian product of n equal 1D PAM constellations (such as square QAM constellations) has the same APE as PAM. The APE of PAM γ_PAM is usually chosen as a benchmark [69, 70], with respect to which the *APE gain* of a constellation is defined as

$$\begin{aligned} g &\triangleq 10 \log_{10} \frac{\gamma}{\gamma_\mathrm{PAM}} \ [\mathrm{dB}] \\ &= g_\mathrm{c} + g_\mathrm{s}. \end{aligned} \tag{3.17}$$

The APE gain can be separated into an *asymptotic coding gain* g_c and an *asymptotic shaping gain* g_s [29]. The coding gain comes from better position arrangement of constellation points over the cubic packing. The shaping gain is obtained by using a more spherical boundary than a hypercubic boundary.

Algorithm 1 Gray penalty calculation

Input: The constellation $\mathcal{X} = \{\boldsymbol{x}_1, \ldots, \boldsymbol{x}_M\}$. Output: Gray penalty G_p.
Preprocessing: Let g^{-1} denote the function that maps a symbol to its bit label.

$counter_1 = 0$
$counter_2 = 0$
for $i = 1, 2, \ldots, M$ **do**
    Find $\mathcal{H} = \{\boldsymbol{h} \in \mathcal{X} : \|\boldsymbol{x}_i - \boldsymbol{h}\| = d_\mathrm{min}\}$
    $counter_1 \leftarrow counter_1 + |\mathcal{H}|$
    $\boldsymbol{c} \leftarrow g^{-1}(\boldsymbol{x}_i)$
    $\mathcal{B} \leftarrow \{g^{-1}(\boldsymbol{h}) : \boldsymbol{h} \in \mathcal{H}\}$
    $counter_2 \leftarrow counter_2 + \sum_{\boldsymbol{b} \in \mathcal{B}} d_\mathrm{H}(\boldsymbol{c}, \boldsymbol{b})$
end for
$G_\mathrm{p} = counter_1 / counter_2$

3.2.4 Gray penalty

To evaluate the labeling rule of a constellation with equally likely points, the Gray penalty G_p is defined as the average number of different bits per pair of symbols at distance d_min [72,73], which can be found in (3.13). The Gray penalty predicts the ratio of the BER P_b to SER P_s at high E_s/N_0 for the AWGN channel:

$$G_\mathrm{p} \approx \frac{mP_\mathrm{b}}{P_\mathrm{s}}. \tag{3.18}$$

Gray-labeled square QAM has the minimum G_p of 1. A pseudocode for calculating the Gray penalty of a constellation is given in Algorithm 1, where d_H denotes the Hamming distance between two binary vectors.

3.2.5 Achievable information rates

The amount of information per symbol that a certain channel can transmit reliably, using a certain modulation format and an encoder/decoder pair, is known as the AIRs [74]. The maximum AIRs including the MI and GMI which serve as fundamental limits of a CM scheme, will be introduced in section 3.4.

Mutual information

The MI between nD random transmitted and received symbols $\boldsymbol{X}$ and $\boldsymbol{Y}$ in Fig. 2.1 is defined as

$$I(\boldsymbol{X}; \boldsymbol{Y}) \triangleq \sum_{\boldsymbol{x} \in \mathcal{X}} p_{\boldsymbol{X}}(\boldsymbol{x}) \int_{\mathbb{R}^n} f_{\boldsymbol{Y}|\boldsymbol{X}}(\boldsymbol{y}|\boldsymbol{x}) \log \frac{f_{\boldsymbol{Y}|\boldsymbol{X}}(\boldsymbol{y}|\boldsymbol{x})}{f_{\boldsymbol{Y}}(\boldsymbol{y})} d\boldsymbol{y}. \tag{3.19}$$

By applying Monte Carlo integration, the MI can be approximated as

$$\begin{aligned} I(\boldsymbol{X};\boldsymbol{Y}) &\approx \frac{1}{N_\mathrm{s}} \sum_{i=1}^{N_\mathrm{s}} \int_{\mathbb{R}^n} f_{\boldsymbol{Y}|\boldsymbol{X}}(\boldsymbol{y}|\boldsymbol{x}^{(i)}) \log \frac{f_{\boldsymbol{Y}|\boldsymbol{X}}(\boldsymbol{y}|\boldsymbol{x}^{(i)})}{f_{\boldsymbol{Y}}(\boldsymbol{y})} d\boldsymbol{y} \\ &\approx \frac{1}{N_\mathrm{s}} \sum_{i=1}^{N_\mathrm{s}} \log \frac{f_{\boldsymbol{Y}|\boldsymbol{X}}(\boldsymbol{y}^{(i)}|\boldsymbol{x}^{(i)})}{f_{\boldsymbol{Y}}(\boldsymbol{y}^{(i)})} \\ &= \frac{1}{N_\mathrm{s}} \sum_{i=1}^{N_\mathrm{s}} \log \frac{f_{\boldsymbol{Y}|\boldsymbol{X}}(\boldsymbol{y}^{(i)}|\boldsymbol{x}^{(i)})}{\frac{1}{M}\sum_{\boldsymbol{x}\in\mathcal{X}} f_{\boldsymbol{Y}|\boldsymbol{X}}(\boldsymbol{y}^{(i)}|\boldsymbol{x})} \end{aligned} \tag{3.20}$$

where $\boldsymbol{x}^{(i)}$ for $i = 1, 2, \ldots, N_\mathrm{s}$ are N_s symbols drawn from $p_{\boldsymbol{X}}(\boldsymbol{x}^{(i)})$, and given a certain $\boldsymbol{x}^{(i)}$, $\boldsymbol{y}^{(i)}$ is drawn from the conditional distribution of the channel $f_{\boldsymbol{Y}|\boldsymbol{X}}(\boldsymbol{y}^{(i)}|\boldsymbol{x}^{(i)})$.

Generalized mutual information

If constellation labeling is considered, the MI between $\boldsymbol{X}$ and $\boldsymbol{Y}$ can also be written as

$$\begin{aligned} I(\boldsymbol{Y};\boldsymbol{X}) &= I(\boldsymbol{Y};B_1,\ldots,B_m) \\ &= I(\boldsymbol{Y};B_1) + I(\boldsymbol{Y};B_2|B_1) + \cdots + I(\boldsymbol{Y};B_m|B_1,\ldots,B_{m-1}) \end{aligned} \tag{3.21}$$

according to the chain rule. Neglecting the conditions of all terms in (3.21) results in a lower bound on it, i.e.,

$$I_{\mathrm{BICM}} \triangleq \sum_{k=1}^{m} I(\boldsymbol{Y};B_k) \leq I(\boldsymbol{Y};\boldsymbol{X}). \tag{3.22}$$

This quantity is called the bit-interleaved coded modulation (BICM) capacity [75, 76]. With the assumption that all bits $B_1, \ldots, B_m$ are independent, which is true for equally likely transmitted symbols, (3.22) is called the GMI [74, Eq. (14)]. Eq. (3.22) can be written as [74, Eq. (16)]

$$\mathrm{GMI} = \frac{1}{M} \sum_{k=1}^{m} \sum_{b\in\{0,1\}} \sum_{\boldsymbol{x}\in\mathcal{X}_k^b} \int_{\mathbb{R}^n} f_{\boldsymbol{Y}|\boldsymbol{X}}(\boldsymbol{y}|\boldsymbol{x}) \log_2 \frac{\frac{1}{M}\sum_{\boldsymbol{x}\in\mathcal{X}_k^b} f_{\boldsymbol{Y}|\boldsymbol{X}}(\boldsymbol{y}|\boldsymbol{x})}{\frac{1}{2} f_{\boldsymbol{Y}}(\boldsymbol{y})} d\boldsymbol{y}, \tag{3.23}$$

where $\mathcal{X}_k^b \subset \mathcal{X}$ is the set of constellation points with a bit b at position k in their m-bit binary label.

The GMI in (3.23) can be approximated by Monte Carlo simulation using N_s channel realization pairs $(\boldsymbol{x}^{(i)}, \boldsymbol{y}^{(i)})$, where $\boldsymbol{x}^{(i)}$ is uniformly and independently drawn from $\mathcal{X}$ at time index i and $\boldsymbol{y}^{(i)}$ is the channel output of $\boldsymbol{x}^{(i)}$ for $i = 1, \ldots, N_\mathrm{s}$. Let the set $\mathcal{Z}_k^b$ denote all indices i of input symbols $\boldsymbol{x}^{(i)}$ that have a bit b at position k. Then (3.23) is

approximated as

$$\begin{aligned}\mathrm{GMI} &\approx \frac{1}{N_\mathrm{s}} \sum_{k=1}^{m} \sum_{b\in\{0,1\}} \sum_{i\in\mathcal{Z}_k^b} \log_2 \frac{\frac{1}{M}\sum_{\boldsymbol{x}\in\mathcal{X}_k^b} f_{\boldsymbol{Y}|\boldsymbol{X}}(\boldsymbol{y}^{(i)}|\boldsymbol{x})}{\frac{1}{2} f_{\boldsymbol{Y}}(\boldsymbol{y}^{(i)})} \\ &= \frac{1}{N_\mathrm{s}} \sum_{k=1}^{m} \sum_{b\in\{0,1\}} \sum_{i\in\mathcal{Z}_k^b} \log_2 \frac{\sum_{\boldsymbol{x}\in\mathcal{X}_k^b} f_{\boldsymbol{Y}|\boldsymbol{X}}(\boldsymbol{y}^{(i)}|\boldsymbol{x})}{\frac{1}{2}\sum_{\boldsymbol{x}\in\mathcal{X}} f_{\boldsymbol{Y}|\boldsymbol{X}}(\boldsymbol{y}^{(i)}|\boldsymbol{x})}. \end{aligned} \tag{3.24}$$

For a certain channel, the MI only depends on the constellation points, whereas the GMI also depends on the constellation labeling. For the nonlinear fiber channel, an auxiliary Gaussian distribution is typically used to replace the $f_{\boldsymbol{Y}|\boldsymbol{X}}(\boldsymbol{y}|\boldsymbol{x})$ in (3.20) and (3.24) [77]. The resulting MI and GMI are lower bounds of the true AIRs for the nonlinear fiber channel.

The MI and GMI can be used to compare different modulation formats and DSP algorithms, and predict data rates and system reach for fiber-optic communication systems. The MI is the a suitable predictor for multilevel coded modulation (MLCM) or nonbinary CM, whereas the GMI is for BICM [74, 78–80].

3.3 Geometric shaping

Shannon's channel capacity is defined as the supremum of the MI under an average power constraint P over all possible input distributions $p_{\boldsymbol{X}}(\boldsymbol{x})$, i.e.,

$$C \triangleq \sup_{p_{\boldsymbol{X}}(\boldsymbol{x}):E_\mathrm{s}\le P} I(\boldsymbol{X};\boldsymbol{Y}). \tag{3.25}$$

For a memoryless AWGN channel, the optimal distribution that maximizes this MI is the Gaussian distribution, whereas the commonly used distribution is a uniform distribution, corresponding to a QAM constellation with equally probable symbols. The asymptotic gap between the uniform distribution and Gaussian distribution is the asymptotic shaping gain g_s in (3.17), which is 1.53 dB[1] [81], as shown in Fig. 3.2. This gap can only be closed by adapting $p_{\boldsymbol{X}}(\boldsymbol{x})$ to the Gaussian distribution, which is called constellation shaping (or signal shaping) in the literature.

GS can be dated back to the 1950's, from two dimensions [25–27] to higher dimensions [69, 82] for the AWGN channel. It aroused intensive interest in the fiber-optic communication community since 2016. MD GS has been performed at low and medium SEs (smaller than approximately 6 bits/2D-symbol) with small constellation cardinalities, relying on different methods, such as machine learning [83–87], and lattices [88–93]. Usually LUTs are needed for encoding and decoding, which is fine with small sizes, but

[1] A strictly uniform input distribution corresponds to square QAM formats with equally likely symbols. Cross QAM formats with equally likely symbols are close to a uniform distribution and I believe their asymptotic gap to the Gaussian distribution is slightly lower than 1.53 dB.

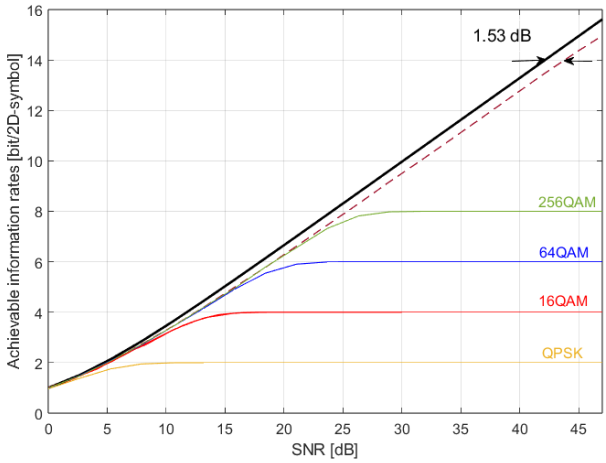

Figure 3.2: The gap between channel capacity and the MI of uniform square QAM constellations for the AWGN channel.

the complexity of the LUT grows exponentially when further increasing the SE. In [94], MD GS was performed at SEs of up to 13 bits/2D-symbol, through machine learning methods utilizing gradient descent algorithms to optimize the GMI, and achieves near-capacity performance.

An alternative GS method is lattice-based VCs. VCs do not need LUTs for encoding and decoding, and the complexity does not increase rapidly with the SE. MD VCs were studied for fiber communications in [95–98] and paper C. In papers A, B, and D, the performance of VCs is investigated for the AWGN channel, but the proposed algorithms are also applicable to nonlinear fiber channels. In [99], VCs are compared with some geometrically shaped constellations through machine learning methods. We will introduce VCs in detail in chapter 4.

For nonlinear fiber channels, shaping might induce a modulation-dependent NLI noise, which is related to the 4th and 6th order moments of the shaped constellations [100,101]. In [100], the impact of shaping on the induced NLI noise is studied for nonlinear fiber channels, and the performance gain found for nonlinear fiber channels is smaller than in the B2B case due to the NLI penalty. However, some shaped constellations are shown to reduce the nonlinear effects [102].

Although shaping techniques can harvest shaping gains, some of them might increase the peak-to-average power ratio (PAPR) over QAM [103–106], which results in performance penalties due to impairments in the optical transmitter, such as the Mach-Zehnder modulator and digital-to-analog converter. Clipping is usually implemented to reduce the PAPR, which might degrade the performance, and can be optimized for systems transmitting shaped constellations [105].

3.4 Coded modulation

FEC coding is a basic component of many wireless and wired communication links, and is a necessity especially when re-transmission is not possible or causes large delay, such as fiber-optic communications, satellite communications, and some use cases in the fifth generation mobile network. Concatenated codes [107, 108], proposed by Forney, where usually an HD outer code and one or several SD inner codes (depending on the CM scheme) are concatenated, are widely used in many communication standards, such as the DVB-S2 [109], 400ZR [5], and 800G standards [92]. The powerful inner codes bring the uncoded BER down to a certain target BER of the outer code (e.g., between 10^{-2} and 10^{-3}). Then, the low-complexity outer code can further eliminate the error floor and achieve a very low post-FEC BER (e.g., 10^{-15} for fiber-optic communications). Competitive inner SD codes can be low-density parity check (LDPC) codes [110], Hamming codes [5, Sec. 10.5], etc. The HD outer codes that have been implemented or are being investigated include Reed–Solomon codes [111], Bose–Chaudhuri–Hocquenghem codes [112], staircase codes [113], turbo product codes [114], zipper codes [115], etc.

Below, some typical CM schemes are introduced. In [80], a nice overview on CM for optical communications is provided.

3.4.1 Multilevel coded modulation

Ungerboeck proposed an MLCM scheme, together with his well-known binary set partitioning (SP) in 1976 [116, 117]. The scheme divides the bit labels into two categories: the least significant bits protected by a convolutional code and the most significant bits being uncoded. Based on the trellis diagram of a convolutional code, the binary SP labeling maps binary labels to 1D or 2D constellation points by successively partitioning the signal set at every bit level such that the intra-set MED is maximized. The Viterbi algorithm [118] is used to decode information bits. This scheme is called trellis-coded modulation [119, 120].

Independently of Ungerboeck's work, Imai *et al.* proposed an MLCM scheme with multistage decoding (MSD) in 1977 [121]. The idea is to protect different bit levels using different binary codes. At the receiver, decoding is performed successively, starting from the least important bit, given the information of all previous bit levels. In Imai's MLCM scheme, any binary FEC code can be used, which is more flexible than trellis-coded modulation. Different partitioning/labeling methods and practical rules of selecting code rates at different levels for this scheme were comprehensively investigated in [122]. Fig. 3.3 illustrates an example of set-partitioning the 16-QAM constellation for all 4 bit levels.

MLCM with MSD is optimal from information theory's perspective, as the underlying criterion is the chain rule. Thus, the MI serves as the upper bound of the AIR of such a CM scheme. However, MLCM has a high complexity due to multiple component codes being used, and MSD induces delay and error propagation when decoding.

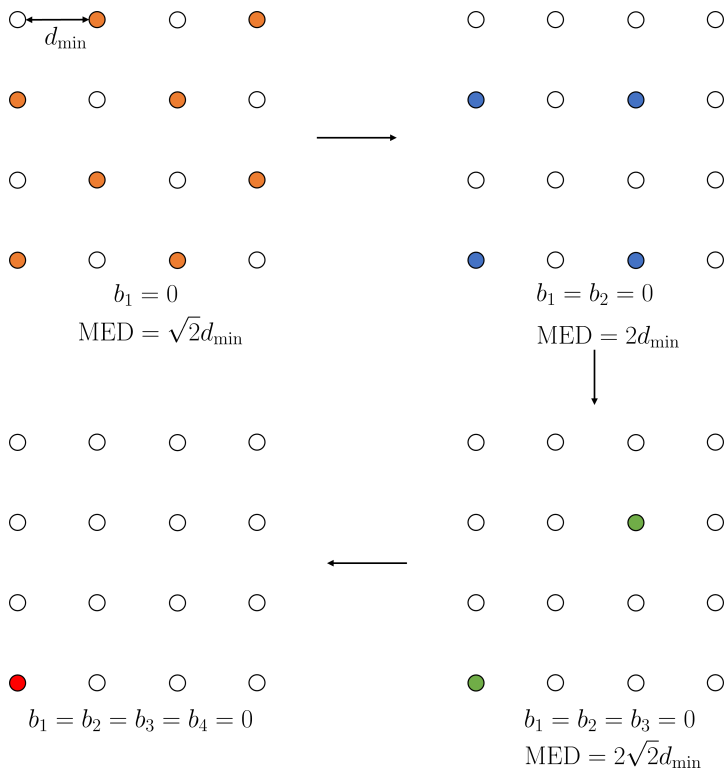

Figure 3.3: An example of set-partitioning the 16-QAM constellation.

3.4.2 Bit-interleaved coded modulation

Proposed by Caire *et al.* in 1998, BICM only uses one component code to protect all bit levels [75]. An interleaver is needed in BICM to avoid burst errors and make all bit levels independent of others. BICM has the advantage of flexibility and low complexity. However, since all bit levels are decoded independently, there is an information loss as explained in (3.22). It has been shown that this loss is small with Gray-labeled constellations [75, 76, 123]. The corresponding upper bound of the AIR with BICM is the GMI. Fig. 3.4 shows the block diagrams of BICM and MLCM with MSD, which are the two CM schemes we consider for VCs in this thesis. SD decoding is assumed and upon receiving a noisy symbol $\boldsymbol{y}$, decoding is based on the LLRs $\boldsymbol{l} = (l_1, \ldots, l_m)$ shown in Fig. 2.1. The LLR value for decoding the k-th bit of $\boldsymbol{y}$ is defined as

$$\begin{aligned} l_k &\triangleq \log \frac{\Pr(b_k = 0|\boldsymbol{y})}{\Pr(b_k = 1|\boldsymbol{y})} \\ &= \log \frac{\sum_{\boldsymbol{x}\in\mathcal{X}_k^0} f_{\boldsymbol{Y}|\boldsymbol{X}}(\boldsymbol{y}|\boldsymbol{x})}{\sum_{\boldsymbol{x}\in\mathcal{X}_k^1} f_{\boldsymbol{Y}|\boldsymbol{X}}(\boldsymbol{y}|\boldsymbol{x})}, \end{aligned} \tag{3.26}$$

where $f_{\boldsymbol{Y}|\boldsymbol{X}}(\boldsymbol{y}|\boldsymbol{x})$ is the channel law. The exact LLR in (3.26) is accurate but computationally complex. A commonly used approximation is the "max-log" approximation [124], where only the most likely constellation point with $b_k = 0$ (or $b_k = 1$) is considered, i.e.,

$$l_k \approx \log \frac{\max_{\boldsymbol{x}\in\mathcal{X}_k^0} f_{\boldsymbol{Y}|\boldsymbol{X}}(\boldsymbol{y}|\boldsymbol{x})}{\max_{\boldsymbol{x}\in\mathcal{X}_k^1} f_{\boldsymbol{Y}|\boldsymbol{X}}(\boldsymbol{y}|\boldsymbol{x})}. \tag{3.27}$$

For the AWGN channel, (3.27) becomes

$$l_k \approx -\frac{1}{2\sigma^2/n}\left(\min_{\boldsymbol{x}\in\mathcal{X}_k^0}(\|\boldsymbol{y}-\boldsymbol{x}\|^2) - \min_{\boldsymbol{x}\in\mathcal{X}_k^1}(\|\boldsymbol{y}-\boldsymbol{x}\|^2)\right), \tag{3.28}$$

which also applies for the nonlinear optical channel with mismatched decoding.

Even with the max-log approximation, LLR calculation is prohibitively complex for very large constellations due to the need of full search in $\mathcal{X}$. To address this issue, we propose a general LLR approximation method for very large constellations with BICM in paper B, based on the concept of importance sampling, where $\mathcal{X}$ in (3.27) is replaced by a much smaller "importance set". In paper D, we propose low-complexity LLR approximation expressions for very large VCs with MLCM, based on lattice partitions.

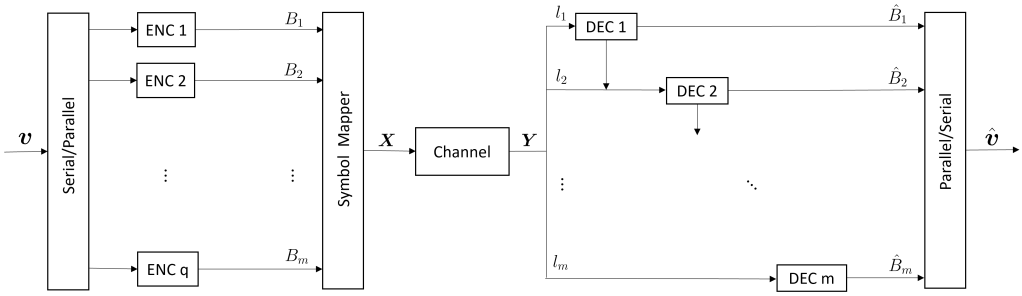

(a) MLCM with MSD

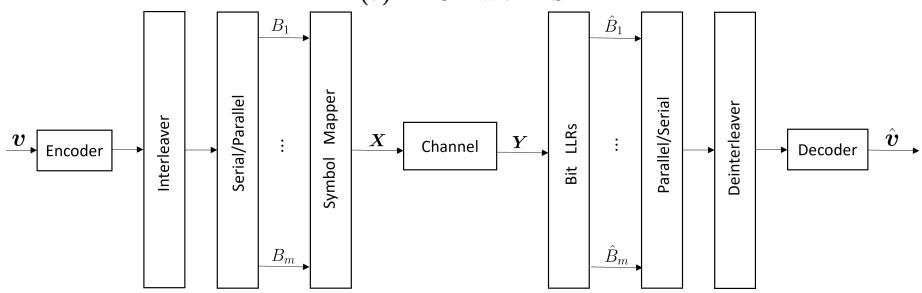

(b) BICM

Figure 3.4: Block diagrams of BICM and MLCM with MSD.

CHAPTER 4

Voronoi Constellations

VCs are lattice-based constellations. In this chapter, we first introduce the basics of lattices and then summarize the design rules, encoding/decoding, labeling methods, and important metrics of VCs.

4.1 Lattices

An nD lattice Λ is a discrete subset of the nD space $\mathbb{R}^n$, generated by its $n \times n$ generator matrix $\boldsymbol{G}_\Lambda$. All linear combinations of the rows of $\boldsymbol{G}_\Lambda$ with all integer coefficients form the lattice

$$\Lambda \triangleq \{\boldsymbol{u}\boldsymbol{G}_\Lambda : \ \boldsymbol{u} \in \mathbb{Z}^n\}. \tag{4.1}$$

The *closest lattice point quantizer* (CLPQ) of a lattice Λ, denoted as $\mathcal{Q}_\Lambda(\ \cdot\ )$, maps an arbitrary point $\boldsymbol{x} \in \mathbb{R}^n$ to its closest lattice point in Λ, i.e.,

$$\mathcal{Q}_\Lambda(\boldsymbol{x}) = \underset{\boldsymbol{\lambda}\in\Lambda}{\arg\min} \|\boldsymbol{x} - \boldsymbol{\lambda}\|^2. \tag{4.2}$$

The *fundamental Voronoi region* of a lattice Λ is the set of vectors in Euclidean space having the all-zero vector as its closest lattice point, i.e.,

$$\Omega(\Lambda) \triangleq \{\boldsymbol{x} \in \mathbb{R}^n : \ \mathcal{Q}_\Lambda(\boldsymbol{x}) = \boldsymbol{0}\}. \tag{4.3}$$

In the following, we introduce the considered lattices in papers A-D and discuss their CLPQ algorithms.

Cubic lattice $\mathbb{Z}^n$

An nD cubic lattice $\mathbb{Z}^n$ is spanned by the n-dimensional identity generator matrix $\boldsymbol{G}_{\mathbb{Z}^n} = \boldsymbol{I}_n$. Finding the closest lattice point in $\mathbb{Z}^n$ of an arbitrary point $\boldsymbol{x} \in \mathbb{R}^n$ is simply rounding every element of $\boldsymbol{x}$ to its nearest integer.

Checkerboard lattice D_n

An nD checkerboard lattice D_n can be obtained from removing half of the points in the cubic lattice $\mathbb{Z}^n$ by performing a parity check, retaining all points in $\mathbb{Z}^n$ with an even sum of the n coordinates, i.e.,

$$D_n = \left\{ \boldsymbol{x} \in \mathbb{Z}^n : \sum_{i=1}^{n} x_i \equiv 0 \pmod 2 \right\}, \tag{4.4}$$

where x_i for $i = 1, \ldots, n$ represents the ith element of a vector $\boldsymbol{x}$. A generator matrix of D_n is

$$\boldsymbol{G}_{D_n} = \begin{pmatrix} 2 & 0 & \cdots & \cdots & 0 \\ 1 & 1 & 0 & \cdots & 0 \\ 1 & 0 & 1 & \ddots & \vdots \\ \vdots & \vdots & \ddots & \ddots & 0 \\ 1 & 0 & \cdots & 0 & 1 \end{pmatrix}. \tag{4.5}$$

A fast algorithm for $\mathcal{Q}_{D_n}(\,\cdot\,)$ is given in [34, Sec. IV].

The cubic lattice can be written as

$$\mathbb{Z}^n = D_n \cup (D_n + \boldsymbol{c}), \tag{4.6}$$

where $\boldsymbol{c}$ is an n-tuple with any one entry being 1 and all other entries being 0.

Gosset lattice E_8

The Gosset lattice is the densest 8D lattice. It is the union of all points in D_8 and their shifted version, i.e.,

$$E_8 = D_8 \cup \left(D_8 + \frac{\mathbf{1}}{\mathbf{2}} \right), \tag{4.7}$$

where $\mathbf{\frac{1}{2}}$ is an 8-tuple with all entries being $\frac{1}{2}$. A generator matrix of E_8 is

$$\boldsymbol{G}_{E_8} = \begin{pmatrix} 2 & 0 & 0 & 0 & 0 & 0 & 0 & 0 \\ 1 & 1 & 0 & 0 & 0 & 0 & 0 & 0 \\ 1 & 0 & 1 & 0 & 0 & 0 & 0 & 0 \\ 1 & 0 & 0 & 1 & 0 & 0 & 0 & 0 \\ 1 & 0 & 0 & 0 & 1 & 0 & 0 & 0 \\ 1 & 0 & 0 & 0 & 0 & 1 & 0 & 0 \\ 1 & 0 & 0 & 0 & 0 & 0 & 1 & 0 \\ \frac{1}{2} & \frac{1}{2} & \frac{1}{2} & \frac{1}{2} & \frac{1}{2} & \frac{1}{2} & \frac{1}{2} & \frac{1}{2} \end{pmatrix}. \tag{4.8}$$

A fast CLPQ algorithm is given in [34, Sec. VI]. For an arbitrary point $\boldsymbol{x} \in \mathbb{R}^n$, the algorithm $\mathcal{Q}_{E_8}(\boldsymbol{x})$ calculates $\mathcal{Q}_{D_8}(\boldsymbol{x})$ and $\mathcal{Q}_{D_8}(\boldsymbol{x} - \mathbf{\frac{1}{2}}) + \mathbf{\frac{1}{2}}$, then returns the one that is closer to $\boldsymbol{x}$.

Barnes–Wall lattice Λ_{16}

The 16-dimensional Barnes–Wall lattice Λ_{16} can be constructed by Construction B [125, Chapter 5] applied to the (16, 5, 8) first-order Reed–Muller code. A detailed description of Λ_{16} can be found in [126]. Its generator matrix is given in [127, Fig. 4]. The lattice Λ_{16} can be written as

$$\Lambda_{16} = \bigcup_{\boldsymbol{c} \in \mathcal{C}} (2D_{16} + \boldsymbol{c}), \tag{4.9}$$

where $\mathcal{C}$ is the set of codewords of the (16, 5, 8) first-order Reed–Muller code and $|\mathcal{C}| = 32$. Thus, similar to $\mathcal{Q}_{E_8}(\boldsymbol{x})$, a fast algorithm of finding the closest point in Λ_{16} performs $\mathcal{Q}_{2D_{16}}(\,\cdot\,)$ 32 times and returns the vector that is closest to $\boldsymbol{x}$, i.e.,

$$\mathcal{Q}_{\Lambda_{16}}(\boldsymbol{x}) = \underset{\boldsymbol{s} \in \mathcal{S}(\boldsymbol{x})}{\arg\min} \|\boldsymbol{s} - \boldsymbol{x}\|^2, \tag{4.10}$$

where

$$\mathcal{S}(\boldsymbol{x}) = \{\boldsymbol{s} = \mathcal{Q}_{2D_{16}}(\boldsymbol{x} - \boldsymbol{c}) + \boldsymbol{c} : \boldsymbol{c} \in \mathcal{C}\}. \tag{4.11}$$

Leech lattice Λ_{24}

A generator matrix of the 24-dimensional Leech lattice Λ_{24} is given in [128, Fig. 5]. The lattice Λ_{24} can be written as

$$\Lambda_{24} = \bigcup_{\boldsymbol{c} \in \mathcal{C}, \boldsymbol{v} \in \mathcal{V}} (4D_{24} + 2\boldsymbol{c} + \boldsymbol{v}), \tag{4.12}$$

where $\mathcal{C}$ is the set of codewords of the (24, 12, 8) Golay code [128] with $|\mathcal{C}| = 4096$ and $\mathcal{V} = \{\mathbf{0}, (-3, 1, 1, \ldots, 1)\}$. Thus, $\mathcal{Q}_{\Lambda_{24}}(\,\cdot\,)$ performs $\mathcal{Q}_{4D_{24}}(\,\cdot\,)$ 8192 times, which is much slower than $\mathcal{Q}_{\Lambda_{16}}(\,\cdot\,)$.

32-dimensional lattice L_{32}

Similar to Λ_{16}, a 32-dimensional lattice can be constructed by applying Construction B, resulting in

$$L_{32} = \bigcup_{\boldsymbol{c}\in\mathcal{C}} (2D_{32} + \boldsymbol{c}), \tag{4.13}$$

where $\mathcal{C}$ is the set of codewords of the (32, 6, 16) first order Reed–Muller code with $|\mathcal{C}| = 64$. Thus, the CLPQ $\mathcal{Q}_{\Lambda_{32}}(\,\cdot\,)$ performs $\mathcal{Q}_{2D_{32}}(\,\cdot\,)$ only 64 times, which is much faster than $\mathcal{Q}_{\Lambda_{24}}(\,\cdot\,)$.

4.2 Design of VCs

4.2.1 Definition

Given an nD lattice Λ and its sublattice Λ_s, the general definition of VC based on the lattice partition $\Lambda/\Lambda_\mathrm{s}$ is defined by Forney in [33] as

$$\Gamma \triangleq (\Lambda - \boldsymbol{a}) \cap \Omega(\Lambda_\mathrm{s}), \tag{4.14}$$

where $\boldsymbol{a} \in \mathbb{R}^n$ is the *offset vector* avoiding VC points falling on the boundary of $\Omega(\Lambda_\mathrm{s})$. The lattice Λ is called the *coding lattice*, which determines the packing structure of VC points, and Λ_s is called the *shaping lattice*, which determines the boundary of the VC. The number of points in the VC is

$$M \triangleq |\Gamma| = \frac{V(\Omega(\Lambda_\mathrm{s}))}{V(\Omega(\Lambda))} = \frac{|\det \boldsymbol{G}_\mathrm{s}|}{|\det \boldsymbol{G}|}, \tag{4.15}$$

where $V(\Omega(\Lambda)) = \int_{\Omega(\Lambda)} dx$ is the volume of the Voronoi region of a lattice Λ, det is the determinant of a matrix, and $\boldsymbol{G}_\mathrm{s}$ and $\boldsymbol{G}$ is the generator matrix of Λ_s and Λ, respectively.

When $\Lambda_\mathrm{s} = k\Lambda$ for some positive integers k, i.e., the shaping lattice is a scaled version of the coding lattice, we call such kind of VC the "scaled VCs" in this thesis, which was first proposed in 1983 by Conway and Sloane in [32]. The performance of scaled VCs was studied for fiber communications in [95–98], showing significant uncoded BER gains over QAM.

Example 1: We consider a 2D VC for which the generator matrices of Λ_s and Λ are

$$\boldsymbol{G}_\mathrm{s} = \begin{pmatrix} 6 & 0 \\ 4 & 4 \end{pmatrix}, \ \boldsymbol{G} = \begin{pmatrix} 1 & 0 \\ 0 & 1 \end{pmatrix}, \tag{4.16}$$

and the offset vector $\boldsymbol{a} = (-1/2, 0)$. Fig. 4.1 illustrates the shifted VC $\Gamma + \boldsymbol{a}$ for convenience.

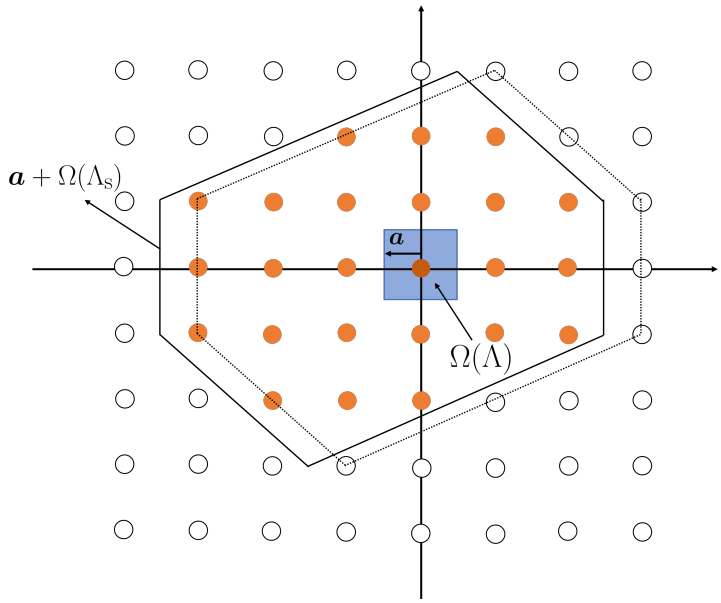

Figure 4.1: A 2D VC in Example 1.

4.2.2 VC parameters

For VCs, the coding gain in (3.17) is obtained by a better coding lattice than the cubic coding lattice and the shaping gain is provided by the shaping lattice. This section discusses the design of the considered VCs in papers A-D.

Shaping lattice Λ_s

The shaping lattice Λ_s should have a high shaping gain. To measure how spherical the shaping lattice is, the normalized second moment of the Voronoi region is a related quantity. Generally, the normalized second moment of an arbitrary region $\mathcal{R}$ is defined as

$$G(\mathcal{R}) = \frac{\int_{\mathcal{R}} \|\boldsymbol{x}\|^2 d\boldsymbol{x}}{nV(\mathcal{R})^{1+2/n}}. \tag{4.17}$$

The normalized second moment of the Voronoi region of the shaping lattice $G(\Omega(\Lambda_s))$ is invariant to scaling and rotation. The cubic lattice has $G(\Omega(\mathbb{Z}^n)) = 1/12$. The smaller the $G(\Omega(\Lambda_s))$, the more spherical the $\Omega(\Lambda_s)$ is, and $G(\Omega(\Lambda_s))$ is lower-bounded by

$$G(\Omega(\Lambda_s)) \geq G(V_n) \xrightarrow{n\to\infty} \frac{1}{2\pi e} \approx 0.0585, \tag{4.18}$$

Table I: Asymptotic shaping gains and normalized second moments of Voronoi regions of some lattices.

Λ_{s}	$\mathbb{Z}^n$	D_4	E_8	Λ_{16}	Λ_{24}	L_{32}
$G(\Omega(\Lambda_{\mathrm{s}}))$	1/12	0.0766	0.0717	0.0683	0.0658	0.0671
$g_{\mathrm{s}}(\Lambda_{\mathrm{s}})$ [dB]	0	0.366	0.653	0.864	1.026	0.935

where V_n is the nD sphere. The asymptotic shaping gain introduced in (3.17) of the shaping lattice Λ_{s} is defined with the reference of the cubic lattice i.e.,

$$g_{\mathrm{s}}(\Lambda_{\mathrm{s}}) = 10\log_{10}\frac{G(\Omega(\mathbb{Z}^n))}{G(\Omega(\Lambda_{\mathrm{s}}))} = 10\log_{10}\frac{1}{12G(\Omega(\Lambda_{\mathrm{s}}))} \leq 1.53 \text{ dB}. \tag{4.19}$$

The shaping gain of some MD lattices is summarized in Table I. The Leech lattice Λ_{24} has the highest asymptotic shaping gain in this table. However, it has the most complex CLPQ algorithm, which dominates the complexity of the encoding and decoding algorithms of VCs. (The encoding and decoding algorithms of VCs will be introduced in Section 4.3.) The 32D lattice L_{32} is a good trade-off between the shaping gain and complexity. In order to achieve high shaping gains, both the number of dimensions and the SE of VCs should be high. VCs tend to be very large under such conditions.

Coding lattice $\mathbb{Z}^n$

In papers A-D, we focus on the cubic coding lattice $\mathbb{Z}^n$, due to the following reasons.

- The CLPQ algorithm of the cubic lattice is much simpler than for other lattices. The complexity of the decoding algorithm of VCs is dominated by the CLPQ algorithm of the coding lattice, which will be discussed in section 4.3.
- The cubic coding lattice has no coding gain. The lack of coding gain can be compensated by FEC codes.
- The small kissing number (the number of the nearest neighbors of a lattice point) of the cubic coding lattices leads to a smaller Gray penalty enabling a more efficient labeling scheme than other coding lattices.
- The simple geometric structure of the cubic coding lattice makes the analysis of important metrics such as the MI, GMI, and LLR feasible for very large VCs, which will be explained in section 4.5.
- The cubic coding lattice doubles the granularity of the SE of VCs compared to scaled VCs, shown as in Eq. (17) in paper B.

Offset vector $\boldsymbol{a}$

A non-zero offset vector can prevent VC points from falling on the boundary of $\Omega(\Lambda_s)$. It can be optimized to minimize the average symbol energy using an iterative algorithm [32]. The procedure is to set an arbitrary and small random $\boldsymbol{a}$ first to get the coordinates of VC points defined in (4.14), then replace the random vector by the centroid of the VC, and restart from (4.14). For 2D and 4D VCs with $M < 131072$, $\boldsymbol{a}$ usually converges to an optimal vector after repeating the above procedure only one time. In the case of 8D VCs, repeating the procedure 3–5 times, $\boldsymbol{a}$ might converge to the optimal vector or a local optimum. The optimization of $\boldsymbol{a}$ is only reasonable for small VCs where all points can be enumerated. For very large VCs, where constellation points can only be generated using Monte Carlo methods, the optimization of $\boldsymbol{a}$ is not possible, and the impact of choosing a random and small $\boldsymbol{a}$ on the average symbol energy is negligible [95, Fig. 3].

In papers A-D, for VCs with $M \leq 2^{17} \approx 1.3 \times 10^5$), $\boldsymbol{a}$ was optimized using the method described in [32], otherwise a random $\boldsymbol{a}$ uniformly distributed in $\Omega(\mathbb{Z}^n)$ was selected.

4.3 Encoding and decoding

The labeling process defined in (3.2) is done for VCs by two steps:

1. Map $m = \log_2(M)$ bits $\boldsymbol{b} \in \{0,1\}^m$ to an integer vector $\boldsymbol{u} \in \mathbb{Z}^n$
2. Map an integer vector $\boldsymbol{u}$ to a VC point $\boldsymbol{x} \in \Gamma$.

Mapping integers to VC points (the second step mentioned above) and vice versa is referred to as encoding and decoding for VCs. For arbitrary VCs, encoding/decoding algorithms are proposed by Feng *et al.* in [129], based on the Smith normal form [130, Ch. 15]. For VCs with a cubic coding lattice, Ferdinand *et al.* proposed encoding and decoding algorithms in [131]. In [37], Kurkoski proposed a "rectangular encoding" method, which is applicable to VCs with a shaping lattice described by a triangular generator matrix and a cubic coding lattice. In this section, the three algorithms are reviewed and compared specifically when they are applied to VCs with a cubic coding lattice.

Table II summarizes the three algorithms for the special case of the lattice partition $\mathbb{Z}^n/\Lambda_s$, which is the focus of papers A-D. The more general versions of Feng's algorithms for arbitrary Λ are described in [129]. In Ferdinand's algorithms described in [131], the basis vectors are column vectors and the decoding goes from low to high dimensions. Here for the convenience of comparison, we describe them using row vectors as basis vectors, and rewrite the decoding process of [131, Eqs. (19)–(21)], with a reverse order of decoding, which however does not change the performance of their algorithms.

Feng's algorithms are more general than Kurkoski's, which are in turn slightly more general than Ferdinand's[1]. However, for the case where all three algorithms are applica-

[1]The $\boldsymbol{dL}$ in Ferdinand's algorithms are not guaranteed to be integer vectors for arbitrary shaping

ble, e.g., for commonly used MD shaping lattices, Kurkoski's algorithms generally make the labeling of VC points easier. Kurkoski's algorithms allow for directly mapping $\boldsymbol{u}$ to constellation points, thus retaining most of the neighbor relationships of constellation points. In Feng's and Ferdinand's encoding algorithms, $\boldsymbol{u}$ is multiplied by a matrix, which changes the neighbor relationships of constellation points.

Example 2: We consider the same VC as in *Example 1* defined in section 4.2.1 and compare different integer mapping rules when Feng's, Ferdinand's, and Kurkoski's algorithms apply to it.

In Feng's algorithms, the Smith normal form $\boldsymbol{J} = \boldsymbol{S}\boldsymbol{G}_{\mathrm{s}}\boldsymbol{T}$ is

$$\boldsymbol{J} = \begin{pmatrix} 2 & 0 \\ 0 & 12 \end{pmatrix}, \ \boldsymbol{S} = \begin{pmatrix} 1 & 1 \\ -2 & -3 \end{pmatrix}, \ \boldsymbol{T} = \begin{pmatrix} 1 & 2 \\ -2 & -5 \end{pmatrix}. \tag{4.20}$$

Then the integer vectors $\boldsymbol{u} = (u_1, u_2)$ are defined as $u_1 \in \{0, 1\}$ and $u_2 \in \{0, \ldots, 11\}$. The vectors $\boldsymbol{u}\boldsymbol{T}^{-1}$ are calculated as

$$\boldsymbol{u}\boldsymbol{T}^{-1} = \begin{pmatrix} u_1 & u_2 \end{pmatrix} \begin{pmatrix} 5 & 2 \\ -2 & -1 \end{pmatrix} = \begin{pmatrix} 5u_1 - 2u_2 & 2u_1 - u_2 \end{pmatrix}. \tag{4.21}$$

In Ferdinand's algorithms, $\boldsymbol{L} = \boldsymbol{G}_{\mathrm{s}}$ and $\boldsymbol{u}$ are enumerated as $u_1 \in \{0, \ldots, 5\}$ and $u_2 \in \{0, \ldots, 3\}$. The vectors $\boldsymbol{d}\boldsymbol{L}$ are computed as

$$\boldsymbol{d}\boldsymbol{L} = \begin{pmatrix} u_1/6 & u_2/4 \end{pmatrix} \begin{pmatrix} 6 & 0 \\ 4 & 4 \end{pmatrix} = \begin{pmatrix} u_1 + u_2 & u_2 \end{pmatrix}. \tag{4.22}$$

In Kurkoski's algorithms, $\boldsymbol{L} = \boldsymbol{G}_{\mathrm{s}}$ and $\boldsymbol{u}$ are enumerated as $u_1 \in \{0, \ldots, 5\}$ and $u_2 \in \{0, \ldots, 3\}$.

Fig. 4.2 illustrates the three different mapping rules for this example, where the vectors $\boldsymbol{u}\boldsymbol{T}^{-1}$ in Feng's algorithms, $\boldsymbol{d}\boldsymbol{L}$ in Ferdinand's algorithms, and $\boldsymbol{u}$ in Kurkoski's algorithms are highlighted. The enumeration of points in a rectangular shape of Kurkoski's algorithms help achieve a lower Gray penalty and a lower BER when the binary reflected Gray code (BRGC) is applied to these integers [paper A].

4.4 Labeling and coded modulation schemes of VCs

As mentioned in section 4.3, the labeling of VCs is two-fold. For the mapping between integers and VC points, we adopt Kurkoski's algorithms described in section 4.3. Thus, designing labeling schemes of VCs focuses on designing the bit-to-integer mapping.

A direct approach is to apply BRGC to the integer vector $\boldsymbol{u}$, resulting in the lowest Gray penalty and best uncoded BER performance. The uncoded and coded BER

lattices, thus making Ferdinand's algorithms less general than Kurkoski's algorithms. The condition for Ferdinand's algorithms to be applicable is $\frac{L_{ij}}{L_{ii}} \in \mathbb{Z}, \forall i = 1, \ldots, n, \ 1 \leq j < i$.

Algorithms	Feng's algorithms [129]	Ferdinand's algorithms [131]	Kurkoski's algorithms [37]
Preprocessing: The generator matrix $\boldsymbol{G}_{\mathrm{s}}$ of the shaping lattice Λ_{s} and the generator matrix of the cubic coding lattice $\boldsymbol{G} = \boldsymbol{I}_n$ are given.	Find two integer matrices $\boldsymbol{S}$ and $\boldsymbol{T}$ with determinant ± 1 such that $\boldsymbol{J} = \boldsymbol{S}\boldsymbol{G}_{\mathrm{s}}\boldsymbol{T}$ is the Smith normal form of $\boldsymbol{G}_{\mathrm{s}}$. Then let $u_i \in \{0, \ldots, J_{ii} - 1\}$ for $i = 1, \ldots, n$.	Find an integer matrix $\boldsymbol{S}$ with determinant ± 1 such that $\boldsymbol{L} = \boldsymbol{S}\boldsymbol{G}_{\mathrm{s}}$ is a lower-triangular matrix with positive diagonal elements. Let $u_i \in \{0, \ldots, L_{ii} - 1\}$ for $i = 1, \ldots, n$.	Find an integer matrix $\boldsymbol{S}$ with determinant ± 1 such that $\boldsymbol{L} = \boldsymbol{S}\boldsymbol{G}_{\mathrm{s}}$ is a lower-triangular matrix with positive diagonal elements (the algorithms are applicable only if $\boldsymbol{L}$ exists). Let $u_i \in \{0, \ldots, L_{ii} - 1\}$ for $i = 1, \ldots, n$.
Encoding: Input $\boldsymbol{u}$. Output $\boldsymbol{x}$.	1) Let $\boldsymbol{c} \leftarrow \boldsymbol{u}\boldsymbol{T}^{-1} - \boldsymbol{a}$ 2) Let $\boldsymbol{z} \leftarrow \mathcal{Q}_{\Lambda_{\mathrm{s}}}(\boldsymbol{c})$ 3) Let $\boldsymbol{x} \leftarrow \boldsymbol{c} - \boldsymbol{z}$	1) Let $\boldsymbol{d} \leftarrow \left(\frac{u_1}{L_{11}}, \frac{u_2}{L_{22}}, \ldots, \frac{u_n}{L_{nn}}\right)$ 2) Let $\boldsymbol{c} = \boldsymbol{d}\boldsymbol{L} - \boldsymbol{a}$ 3) Let $\boldsymbol{z} \leftarrow \mathcal{Q}_{\Lambda_{\mathrm{s}}}(\boldsymbol{c})$ 4) Let $\boldsymbol{x} \leftarrow \boldsymbol{c} - \boldsymbol{z}$	1) Let $\boldsymbol{c} \leftarrow \boldsymbol{u} - \boldsymbol{a}$ 2) Let $\boldsymbol{z} \leftarrow \mathcal{Q}_{\Lambda_{\mathrm{s}}}(\boldsymbol{c})$ 3) Let $\boldsymbol{x} \leftarrow \boldsymbol{c} - \boldsymbol{z}$
Decoding: Input $\boldsymbol{y}$. Output $\boldsymbol{u}$.	1) Let $\boldsymbol{c} \leftarrow \lfloor \boldsymbol{y} + \boldsymbol{a} \rceil$ 2) Let $\boldsymbol{u} \leftarrow \boldsymbol{c}\boldsymbol{T}$ 3) Let $u_i \leftarrow u_i \mod J_{ii}$, $\forall i = 1, \ldots, n$	1) Let $\boldsymbol{u} \leftarrow \lfloor \boldsymbol{y} + \boldsymbol{a} \rceil$ 2) For $i = n, n-1, \ldots, 1$, do $\begin{cases} v_i \leftarrow \lfloor u_i / L_{ii} \rfloor \\ \boldsymbol{u} \leftarrow \boldsymbol{u} - v_i \boldsymbol{l}_i \end{cases}$	1) Let $\boldsymbol{u} \leftarrow \lfloor \boldsymbol{y} + \boldsymbol{a} \rceil$ 2) for $i = n, n-1, \ldots, 1$, do $\begin{cases} v_i \leftarrow \lfloor u_i / L_{ii} \rfloor \\ \boldsymbol{u} \leftarrow \boldsymbol{u} - v_i \boldsymbol{l}_i \end{cases}$

Table II: A Comparison of different encoding and decoding algorithms for VCs with a cubic coding lattice.

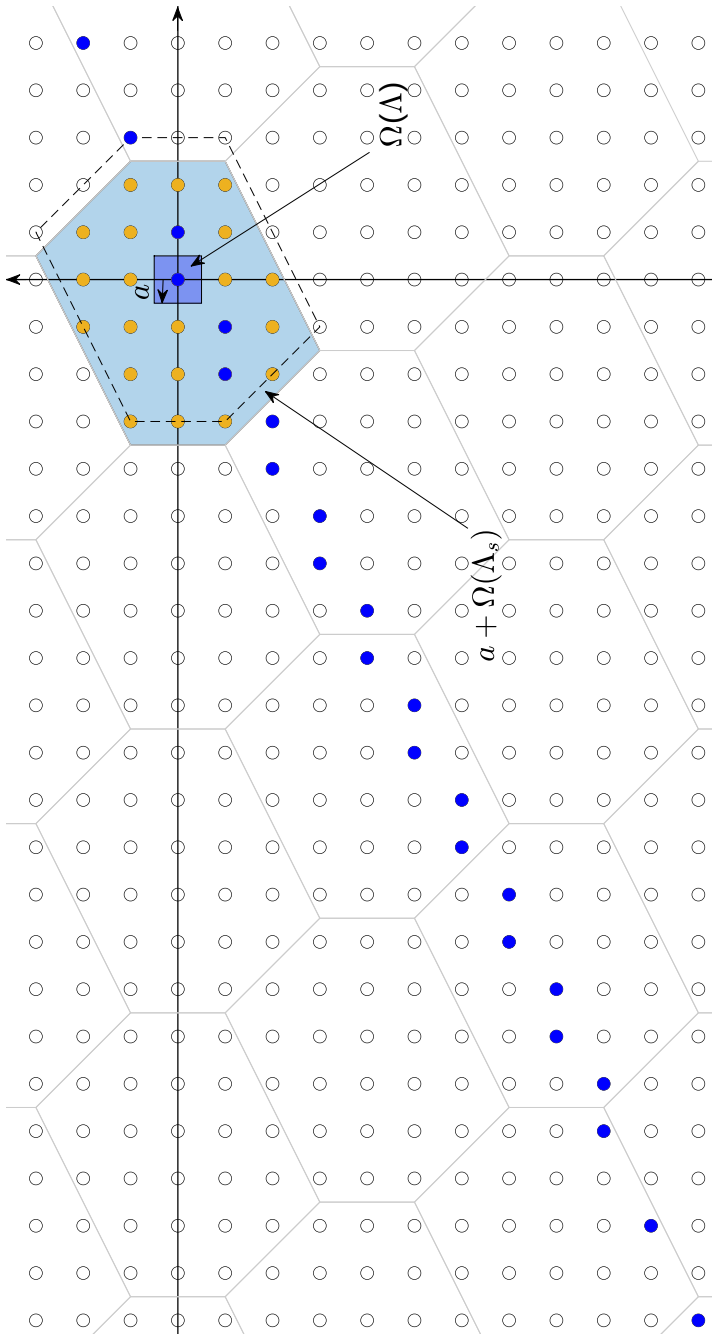

(a) Ferdinand's algorithms.

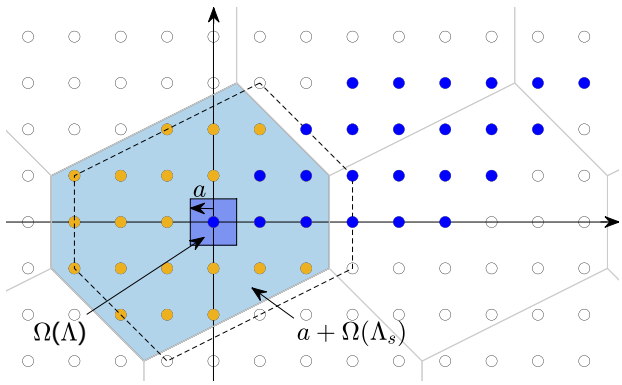

(b) Ferdinand's algorithms.

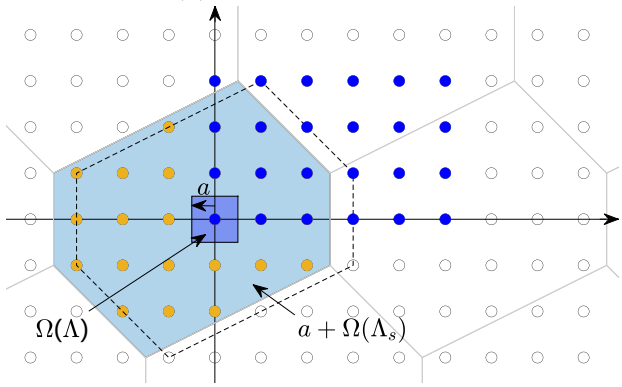

(c) Kurkoski's algorithms.

Figure 4.2: Example 2: different integer mapping rules for a 2D VC. The blue filled points are encoded into points in the shifted Voronoi region $\boldsymbol{a} + \Omega(\Lambda_s)$ (the light blue region) in encoding.

performance, adopting the Gray bit-to-integer mapping, is shown in paper A and D, respectively.

Another mapping idea is inspired by Ungerboeck's binary SP introduced in section 3.4.1. Binary SP has been applied to 1D, 2D [122, 132, 133], and 4D [92, 93, 134, 135] signal constellations. When binary SP is applied in dimensions larger than 2, the intra-set MED might not increase at every bit level [134]. Binary SP also requires one FEC encoder/decoder pair at each bit level, which has a large encoding/decoding complexity if the number of partition steps is large, and the delay introduced in multistage decoding is proportional to the number of FEC encoder/decoder pairs. Generalized from the binary SP, signal sets can be partitioned into multiple subsets based on the concept of cosets [33,82,136,137], which enables SP in higher dimensions [33,82,137] and increasing MED at every partition level. In paper D, we propose an "SP mapping" algorithm and a special case thereof named "hybrid mapping" for VCs based on the SP with cosets. The BER performance of VCs adopting these mapping rules in both uncoded and coded systems have been studied and compared with QAM.

Although VCs offer high shaping gains, designing CM schemes for VCs to outperform Gray-labeled QAM[2] is challenging. This is due to the absence of Gray labeling for VCs, and the resulting penalty from a non-Gray labeling might cancel out the shaping gain of VCs. Both BICM and MLCM for VCs with SD FEC codes are designed in paper D, and were indeed shown to outperform Gray-labeled QAM with BICM.

4.5 MI, GMI, and LLRs for very large VCs

Analyzing the MI and GMI of VCs helps with system design, and LLRs are necessary for VCs with SD decoding. However, by definitions (3.20), (3.24), and (3.27), the calculation of the MI and GMI requires full enumeration of all constellation points, which becomes infeasible for large values of M. To address this challenge, we proposed a general MI estimation method and an LLR approximation method for very large constellations based on *importance sampling* in paper B. The MI estimation method is then generalized to estimating the GMI in paper C. In the following, the concept of classical importance sampling is briefly introduced.

Importance sampling is a weighted sampling method used in statistics for estimating properties of a target distribution [138, Ch. 9]. It proves particularly useful when generating samples from a known distribution is challenging, e.g., the inverse of the cumulative density function of the distribution is hard to get, or the Monte Carlo method breaks down, which is the case in the following example. This method has applications in various areas, including Bayesian inference, Monte Carlo simulation, and rare event simulation.

[2] Gray labeling for cross QAM does not exist [73]. For cross QAM, usually a "quasi-Gray" labeling is adopted [72]. In this thesis, "Gray-labeled QAM" loosely refers to both Gray-labeled square QAM and quasi-Gray-labeled cross QAM formats.

For instance, suppose the problem is to estimate the expectation

$$\mathbb{E}[g(\boldsymbol{X})] = \int_A f_{\boldsymbol{X}}(x) g(x) \, \mathrm{d}x \tag{4.23}$$

for a random variable $\boldsymbol{X}$, where $g(x)$ is a function of x, $f_{\boldsymbol{X}}(x)$ is the probability density function of $\boldsymbol{X}$, and A is the integral interval. When the Monte Carlo method breaks down, e.g., the samples having the most significant contribution to the value of $g(x)$ are in the tail of $f_{\boldsymbol{X}}(x)$, importance sampling can solve this issue by properly introducing another distribution $q_{\boldsymbol{X}}(x)$ to make Monte Carlo methods feasible again. Then the expectation can be rewritten as

$$\mathbb{E}[g(\boldsymbol{X})] = \int_A f_{\boldsymbol{X}}(x) g(x) \, \mathrm{d}x = \int_A g(x) \frac{f_{\boldsymbol{X}}(x)}{q_{\boldsymbol{X}}(x)} q_{\boldsymbol{X}}(x) \, \mathrm{d}x. \tag{4.24}$$

Applying Monte Carlo integration to (4.24) yields

$$\mathbb{E}[g(\boldsymbol{X})] \approx \frac{1}{N} \sum_{n=1}^{N} g(x_n) \frac{f_{\boldsymbol{X}}(x_n)}{q_{\boldsymbol{X}}(x_n)}, \tag{4.25}$$

where x_n for $n = 1, \ldots, N$ are N samples from the distribution $q_{\boldsymbol{X}}$. The key point is to choose this $q_{\boldsymbol{X}}$. Generally, $q_{\boldsymbol{X}}(x)$ is proportional to $|f_{\boldsymbol{X}}(x)|g(x)$ [139].

CHAPTER 5

Contributions and Future Work

In this chapter, we summarize our research flow and the contributions of the appended papers, and discuss the future work.

5.1 Paper A

In paper A, we conducted a study on three existing encoding and decoding algorithms for VCs in the literature: Feng's, Kurkoski's, and Ferdinand's algorithms (summarized in section 4.3). According to their different characteristics, we propose the use of VCs with a cubic coding lattice adopting Kurkoski's algorithms, with a pseudo-Gray labeling. Such VCs have the same theoretical shaping gains but lower decoding complexity and better labeling schemes than classical VCs. Simulation results over the AWGN channel show that the proposed VCs achieve the lowest uncoded BER. An LDPC code is applied to medium large VCs (with less than 131072 constellation points), showing that the designed VCs have the lowest BER after LDPC decoding. Furthermore, we propose a Gray penalty estimation method for very large VCs with a cubic coding lattice to evaluate different labeling schemes.

Contributions: Shen Li (SL) compared the encoding/decoding algorithms, proposed the Gray penalty estimation method, performed the simulation, analyzed the results, and wrote the paper. Erik Agrell (EA) and Magnus Karlsson (MK) proposed the research idea and formulated the problem. Ali Mirani (AM) contributed to the analysis. All authors reviewed and revised the paper.

Context: section 4.3.

5.2 Paper B

In paper B, we propose an MI estimation method and an LLR approximation method for very large constellations based on importance sampling, and apply them to the designed VCs with up to 3.6×10^{75} constellation points. The MI of VCs is estimated accurately for the AWGN channel, showing high shaping gains over QAM formats in the medium and high E_s/N_0 range. The LLR approximation method makes applying an SD FEC code on top of such VCs feasible, and good coded BER results are found when the code rate is high. The simulation results over the AWGN channel imply that VCs have good potential for nonlinear fiber channels.

Contributions: SL proposed the LLR approximation method, performed the simulation, contributed to the MI estimation algorithm, analyzed the results, and wrote the paper. EA formulated the problem, proposed the importance sampling idea of estimating the MI, and contributed to the analysis. AM and MK contributed to the analysis. All authors reviewed and revised the paper.

Context: section 4.5.

5.3 Paper C

The good BER and MI performance of VCs over the AWGN channel found in papers A and B encourage the investigation of their application in fiber-optic communication systems. In paper C, we focus on VC transmission over nonlinear fiber channels, including the B2B, single-channel, and WDM systems. The fiber transmission is simulated using the SSFM to solve the dual-polarized Manakov equation. The received DSP schemes include CD compensation and DBP. We also proposed a general GMI estimation method for very large constellations, extended from the MI estimation method in paper B. We compare the uncoded BER, MI, and GMI performance of VCs with QAM in fiber communication systems. The observed uncoded BER gains of VCs over QAM show that VCs can achieve better performance than QAM in systems with HD FEC decoding. The GMI gains are observed only at high SEs and when the GMI is above 0.9 of the SE, which indicates that one suitable CM for VCs is BICM with high code rates and the SE of VCs should be high. The MI gains suggest that MLCM for VCs is worth investigating.

Contributions: SL generalized the GMI estimation method, designed the simulation, analyzed the results, and wrote the paper. AM and MK provided guidance on fiber channel simulation. EA contributed to the analysis. All authors reviewed and revised the paper.

Context: section 4.5.

5.4 Paper D

The high MI and GMI performance of VCs demonstrated in papers B and C suggests potential gains of VCs over QAM in coded systems. Practical CM schemes are needed to preserve the VCs' high shaping gains. In paper D, we design a concatenated CM scheme, combining inner BICM and MLCM schemes with SD codes and outer HD codes for very large VCs. For the inner MLCM, we propose two new bit-to-integer algorithms of VCs based on lattice partition chains, and the corresponding LLR calculation algorithms. This makes very large VCs adoptable in practical communication systems using SD FEC codes with low complexity. The simulation results using LDPC codes for the AWGN channel show that the proposed CM schemes sustain good shaping gains of VCs over QAM in both BICM and MLCM schemes.

Contributions: SL formulated the problem, designed the CM schemes, labeling algorithms, and LLR calculation algorithms for VCs. EA contributed to the analysis. All authors reviewed and revised the paper.

Context: section 4.4.

5.5 Future work

- **VC transmission over nonlinear fiber channels using the designed CM schemes in paper D**

Paper D has shown the excellent BER performance of VCs after LDPC decoding in the AWGN channel. Paper C has shown higher uncoded BER, MI, and GMI gains of VCs in nonlinear fiber channels than for the AWGN channel. Thus, higher E_s/N_0 gains of VCs over QAM after LDPC decoding are expected for nonlinear fiber channels.

- **Optimization of FEC codes for VC transmission over nonlinear fiber channels**

For the upcoming next-generation 800 Gbps and 1.6 Tbps standards for fiber communications, different types of FEC codes and specific DSP techniques can be investigated and optimized for VCs to propose a tailored solution.

- **Comparing VCs with other GS methods**

For the optical channel, a fair comparison of VCs with other GS methods, including machine learning and shaping for lattice codes, is currently lacking. Comparisons can be made in terms of MI, GMI, complexity, and modulation-dependent distortions induced by shaped constellations.

Bibliography

[1] S. Tsukamoto, D.-S. Ly-Gagnon, K. Katoh, and K. Kikuchi, "Coherent demodulation of 40-Gbit/s polarization-multiplexed QPSK signals with 16-GHz spacing after 200-km transmission," in *Proc. Opt. Fiber Commun. Conf. (OFC)*, Anaheim, CA, USA, March 2005.

[2] H. Sun, K.-T. Wu, and K. Roberts, "Real-time measurements of a 40 Gb/s coherent system," *Opt. Exp.*, vol. 16, no. 2, pp. 873–879, Jan 2008.

[3] E. Ip and J. M. Kahn, "Compensation of dispersion and nonlinear impairments using digital backpropagation," *J. Lightw. Technol.*, vol. 26, no. 20, pp. 3416–3425, 2008.

[4] M. G. Ahmed, T. N. Huynh, C. Williams, Y. Wang, R. Shringarpure, R. Yousefi, J. Roman, N. Ophir, and A. Rylyakov, "A 34Gbaud linear transimpedance amplifier with automatic gain control for 200Gb/s DP-16QAM optical coherent receivers," in *Proc. Opt. Fiber Commun. Conf. (OFC)*, San Diego, CA, USA, March 2018.

[5] Optical Internetworking Forum, "OIF-400ZR-01.0 – implementation agreement 400ZR," https://www.oiforum.com/wp-content/uploads/OIF-400ZR-01.0_reduced2.pdf, March 2020.

[6] "Maximizing the capacity reach of 800G generation coherent: Baud rates, features, and modem SNR." [Online]. Available: https://www.infinera.com/wp-content/uploads/Maximizing-the-Capacity-Reach-of-800G-Generation-Coherent-0271-WP-RevA-0920.pdf

[7] "5G; NR; Physical channels and modulation (3GPP TS 38.211 version 16.2.0 Release 16)," ETSI TS 138 211 V16.2.0 (2020-07). [Online]. Available: https://www.etsi.org/deliver/etsi_ts/138200_138299/138211/16.02.00_60/ts_138211v160200p.pdf

[8] "Digital video broadcasting (DVB); Implementation guidelines for a second generation digital terrestrial television broadcasting system (DVB-T2)," ETSI TS

102 831 V1.2.1 (2012-08). [Online]. Available: https://www.etsi.org/deliver/etsi_ts/102800_102899/102831/01.02.01_60/ts_102831v010201p.pdf

[9] V. Bajaj, F. Buchali, M. Chagnon, S. Wahls, and V. Aref, "Single-channel 1.61 Tb/s optical coherent transmission enabled by neural network-based digital pre-distortion," in *Proc. Eur. Conf. Opt. Commun. (ECOC)*, Brussels, Belgium, Dec. 2020.

[10] F. Pittalà, R.-P. Braun, G. Böcherer, P. Schulte, M. Schaedler, S. Bettelli, S. Calabrò, M. Kuschnerov, A. Gladisch, F.-J. Westphal, C. Xie, R. Chen, Q. Wang, and B. Zheng, "1.71 Tb/s single-channel and 56.51 Tb/s DWDM transmission over 96.5 km field-deployed SSMF," *IEEE Photon. Technol. Lett.*, vol. 34, no. 3, pp. 157–160, 2022.

[11] F. Buchali, V. Aref, R. Dischler, M. Chagnon, K. Schuh, H. Hettrich, A. Bielik, L. Altenhain, M. Guntermann, R. Schmid, and M. Möller, "128 GSa/s SiGe DAC implementation enabling 1.52 Tb/s single carrier transmission," *J. Lightw. Technol.*, vol. 39, no. 3, pp. 763–770, 2021.

[12] S. Kaimalettu, A. Thangaraj, M. Bloch, and S. W. McLaughlin, "Constellation shaping using LDPC codes," in *Proc. IEEE Int. Symp. Inf. Theory (ISIT)*, Nice, France, June 2007, pp. 2366–2370.

[13] N. S. Ferdinand, B. M. Kurkoski, M. Nokleby, and B. Aazhang, "Low-dimensional shaping for high-dimensional lattice codes," *IEEE Trans. Wireless Commun.*, vol. 15, no. 11, pp. 7405–7418, 2016.

[14] B. M. Kurkoski, J. Dauwels, and H.-A. Loeliger, "Power-constrained communications using LDLC lattices," in *Proc. IEEE Int. Symp. Inf. Theory (ISIT)*, Seoul, Korea, July 2009.

[15] G. Böcherer, F. Steiner, and P. Schulte, "Bandwidth efficient and rate-matched low-density parity-check coded modulation," *IEEE Trans. Commun.*, vol. 63, no. 12, pp. 4651–4665, 2015.

[16] F. Buchali, F. Steiner, G. Böcherer, L. Schmalen, P. Schulte, and W. Idler, "Rate adaptation and reach increase by probabilistically shaped 64-QAM: An experimental demonstration," *J. Lightw. Technol.*, vol. 34, no. 7, pp. 1599–1609, 2016.

[17] S. Chandrasekhar, B. Li, J. Cho, X. Chen, E. Burrows, G. Raybon, and P. Winzer, "High-spectral-efficiency transmission of PDM 256-QAM with parallel probabilistic shaping at record rate-reach trade-offs," in *Proc. Eur. Conf. Opt. Commun. (ECOC)*, Dusseldorf, Germany, Sept. 2016.

[18] M. P. Yankov, F. Da Ros, E. P. da Silva, S. Forchhammer, K. J. Larsen, L. K. Oxenløwe, M. Galili, and D. Zibar, "Constellation shaping for WDM systems using

256QAM/1024QAM with probabilistic optimization," *J. Lightw. Technol.*, vol. 34, no. 22, pp. 5146–5156, 2016.

[19] J. Cho and P. J. Winzer, "Probabilistic constellation shaping for optical fiber communications," *J. Lightw. Technol.*, vol. 37, no. 6, pp. 1590–1607, 2019.

[20] R. T. Jones, T. A. Eriksson, M. P. Yankov, and D. Zibar, "Deep learning of geometric constellation shaping including fiber nonlinearities," in *Proc. Eur. Conf. Opt. Commun. (ECOC)*, Rome, Italy, Sept. 2018.

[21] B. Chen, Y. Lei, G. Liga, Z. Liang, W. Ling, X. Xue, and A. Alvarado, "Geometrically-shaped multi-dimensional modulation formats in coherent optical transmission systems," *J. Lightw. Technol.*, vol. 41, no. 3, pp. 897–910, 2023.

[22] "Nokia PSE-V technical white paper." [Online]. Available: https://onestore.nokia.com/asset/207220

[23] "1FINITY T600 transport blade." [Online]. Available: https://www.fujitsu.com/us/Images/1FINITY-T600-Data-Sheet.pdf

[24] F. A. Aoudia and J. Hoydis, "Joint learning of probabilistic and geometric shaping for coded modulation systems," in *Proc. IEEE Glob. Commun. Conf. (GLOBECOM)*, Taipei, Taiwan, Dec. 2020.

[25] E. N. Gilbert, "A comparison of signalling alphabets," *Bell Syst. Tech. J.*, vol. 31, no. 3, pp. 504–522, 1952.

[26] C. N. Campopiano and B. G. Glazer, "A coherent digital amplitude and phase modulation scheme," *IRE Trans. Commun. Sys.*, vol. 10, no. 1, pp. 90–95, 1962.

[27] G. J. Foschini, R. D. Gitlin, and S. Weinstein, "Optimization of two-dimensional signal constellations in the presence of Gaussian noise," *IEEE Trans. Commun.*, vol. 22, no. 1, pp. 28–38, 1974.

[28] E. Agrell, "Database of sphere packings." [Online]. Available: https://codes.se/packings/

[29] E. Agrell and M. Karlsson, "Power-efficient modulation formats in coherent transmission systems," *J. Lightw. Technol.*, vol. 27, no. 22, pp. 5115–5126, 2009.

[30] P. Schulte and G. Böcherer, "Constant composition distribution matching," *IEEE Trans. Inf. Theory*, vol. 62, no. 1, pp. 430–434, 2016.

[31] F. Steiner and G. Böecherer, "Comparison of geometric and probabilistic shaping with application to ATSC 3.0," in *Proc. Int. ITG Conf. Sys., Commun., and Coding*, Hamburg, Germany, Feb. 2017.

[32] J. H. Conway and N. J. A. Sloane, "A fast encoding method for lattice codes and quantizers," *IEEE Trans. Inf. Theory*, vol. IT-29, no. 6, pp. 820–824, 1983.

[33] G. D. Forney, Jr., "Multidimensional constellations—part II: Voronoi constellations," *IEEE J. Sel. Areas Commun.*, vol. 7, no. 6, pp. 941–958, 1989.

[34] J. H. Conway and N. J. A. Sloane, "Fast quantizing and decoding algorithms for lattice quantizers and codes," *IEEE Trans. Inf. Theory*, vol. IT-28, no. 2, pp. 227–232, 1982.

[35] N. Sommer, M. Feder, and O. Shalvi, "Shaping methods for low-density lattice codes," in *Proc. IEEE Inf. Theory Workshop (ITW)*, Taormina, Italy, Oct. 2009.

[36] R. Zamir, "How to design an efficient lattice coding scheme," in *Proc. IEEE Inf. Theory Workshop (ITW)*, Hobart, Australia, Nov. 2014.

[37] B. M. Kurkoski, "Encoding and indexing of lattice codes," *IEEE Trans. Inf. Theory*, vol. 64, no. 9, pp. 6320–6332, 2018.

[38] U. Erez and R. Zamir, "Achieving $1/2 \log(1 + \mathrm{SNR})$ on the AWGN channel with lattice encoding and decoding," *IEEE Trans. Inf. Theory*, vol. 50, no. 10, pp. 2293–2314, 2004.

[39] N. di Pietro, G. Zémor, and J. J. Boutros, "LDA lattices without dithering achieve capacity on the Gaussian channel," *IEEE Trans. Inf. Theory*, vol. 64, no. 3, pp. 1561–1594, 2018.

[40] N. di Pietro and J. J. Boutros, "Leech constellations of construction-A lattices," *IEEE Trans. Commun.*, vol. 65, no. 11, pp. 4622–4631, 2017.

[41] P. R. Branco da Silva and D. Silva, "Multilevel LDPC lattices with efficient encoding and decoding and a generalization of construction D$'$," *IEEE Trans. Inf. Theory*, vol. 65, no. 5, pp. 3246–3260, 2019.

[42] H. Buglia and R. R. Lopes, "Voronoi shaping for lattices with efficient encoding," *IEEE Commun. Lett.*, vol. 25, no. 5, pp. 1439–1442, 2021.

[43] F. Zhou and B. M. Kurkoski, "Construction D$'$ lattices for power-constrained communications," *IEEE Trans. Commun.*, vol. 70, no. 4, pp. 2200–2212, 2022.

[44] P. K. A. Wai, C. R. Menyuk, and H. H. Chen, "Stability of solitons in randomly varying birefringent fibers," *Opt. Lett.*, vol. 16, no. 16, pp. 1231–1233, Aug 1991.

[45] S. J. Savory, "Digital filters for coherent optical receivers," *Opt. Exp.*, vol. 16, no. 2, pp. 804–817, Jan 2008.

[46] G. Goldfarb and G. Li, "Chromatic dispersion compensation using digital IIR filtering with coherent detection," *IEEE Photon. Technol. Lett.*, vol. 19, no. 13, pp. 969–971, 2007.

[47] E. Agrell, "Capacity bounds in optical communications," in *Proc. Eur. Conf. Opt. Commun. (ECOC)*, Gothenburg, Sweden, Sept. 2017.

[48] K. Keykhosravi, "Capacity analysis and receiver design in the presence of fiber nonlinearity," *Doctoral thesis, Chalmers Univ. of Tech.*, 2019.

[49] S. Musetti, P. Serena, and A. Bononi, "On the accuracy of split-step Fourier simulations for wideband nonlinear optical communications," *J. Lightw. Technol.*, vol. 36, no. 23, pp. 5669–5677, 2018.

[50] O. V. Sinkin, R. Holzlohner, J. Zweck, and C. R. Menyuk, "Optimization of the split-step Fourier method in modeling optical-fiber communications systems," *J. Lightw. Technol.*, vol. 21, no. 1, pp. 61–68, 2003.

[51] Q. Zhang and M. I. Hayee, "Symmetrized split-step Fourier scheme to control global simulation accuracy in fiber-optic communication systems," *J. Lightw. Technol.*, vol. 26, no. 2, pp. 302–316, 2008.

[52] A. M. Heidt, "Efficient adaptive step size method for the simulation of supercontinuum generation in optical fibers," *J. Lightw. Technol.*, vol. 27, no. 18, pp. 3984–3991, 2009.

[53] J. Shao, X. Liang, and S. Kumar, "Comparison of split-step Fourier schemes for simulating fiber optic communication systems," *IEEE Photon. J.*, vol. 6, no. 4, pp. 1–15, 2014.

[54] S. Li, M. Karlsson, and E. Agrell, "Improved simulation accuracy of the split-step Fourier method," in *Proc. Opt. Fiber Commun. Conf. (OFC)*, San Deigo, USA, March 2020, pp. W2A–55.

[55] Y. Zhu and D. V. Plant, "Optimal design of dispersion filter for time-domain split-step simulation of pulse propagation in optical fiber," *J. Lightw. Technol.*, vol. 30, no. 10, pp. 1405–1421, 2012.

[56] K. Roberts, C. Li, L. Strawczynski, M. O'Sullivan, and I. Hardcastle, "Electronic precompensation of optical nonlinearity," *IEEE Photon. Technol. Lett.*, vol. 18, no. 2, pp. 403–405, 2006.

[57] E. Temprana, E. Myslivets, B. P.-P. Kuo, N. Alic, and S. Radic, "Transmitter-side digital back propagation with optical injection-locked frequency referenced carriers," *J. Lightw. Technol.*, vol. 34, no. 15, pp. 3544–3549, 2016.

[58] L. B. Du and A. J. Lowery, "Improved single channel backpropagation for intra-channel fiber nonlinearity compensation in long-haul optical communication systems," *Opt. Exp.*, vol. 18, no. 16, pp. 17 075–17 088, 2010.

[59] D. Lavery, D. Ives, G. Liga, A. Alvarado, S. J. Savory, and P. Bayvel, "The benefit of split nonlinearity compensation for single-channel optical fiber communications," *IEEE Photon. Technol. Lett.*, vol. 28, no. 17, pp. 1803–1806, 2016.

[60] C. Häger and H. D. Pfister, "Deep learning of the nonlinear Schrödinger equation in fiber-optic communications," in *Proc. IEEE Int. Symp. Inf. Theory (ISIT)*, San Diego, CA, 2018, pp. 1590–1594.

[61] Y. Gao, J. H. Ke, J. C. Cartledge, K. P. Zhong, and S. S.-H. Yam, "Implication of parameter values on low-pass filter assisted digital back propagation for DP 16-QAM," *IEEE Photon. Technol. Lett.*, vol. 25, no. 10, pp. 917–920, 2013.

[62] S. Li, M. Karlsson, and E. Agrell, "Antialiased transmitter-side digital backpropagation," *IEEE Photon. Technol. Lett.*, vol. 32, no. 18, pp. 1211–1214, 2020.

[63] N. V. Irukulapati, D. Marsella, P. Johannisson, E. Agrell, M. Secondini, and H. Wymeersch, "Stochastic digital backpropagation with residual memory compensation," *J. Lightw. Technol.*, vol. 34, no. 2, pp. 566–572, Jan 2016.

[64] P. Poggiolini, G. Bosco, A. Carena, V. Curri, Y. Jiang, and F. Forghieri, "The GN-model of fiber non-linear propagation and its applications," *J. Lightw. Technol.*, vol. 32, no. 4, pp. 694–721, 2014.

[65] A. Nespola, S. Straullu, A. Carena, G. Bosco, R. Cigliutti, V. Curri, P. Poggiolini, M. Hirano, Y. Yamamoto, T. Sasaki, J. Bauwelinck, K. Verheyen, and F. Forghieri, "GN-model validation over seven fiber types in uncompensated PM-16QAM Nyquist-WDM links," *IEEE Photon. Technol. Lett.*, vol. 26, no. 2, pp. 206–209, Jan. 2014.

[66] E. Torrengo, R. Cigliutti, G. Bosco, A. Carena, V. Curri, P. Poggiolini, A. Nespola, D. Zeolla, and F. Forghieri, "Experimental validation of an analytical model for non-linear propagation in uncompensated optical links," *Opt. Exp.*, vol. 19, no. 26, pp. B790–B798, 2011.

[67] R. Dar, M. Feder, A. Mecozzi, and M. Shtaif, "Properties of nonlinear noise in long, dispersion-uncompensated fiber links," *Opt. Exp.*, vol. 21, no. 22, pp. 25 685–25 699, Nov. 2013.

[68] A. Carena, G. Bosco, V. Curri, Y. Jiang, P. Poggiolini, and F. Forghieri, "EGN model of non-linear fiber propagation," *Opt. Exp.*, vol. 22, no. 13, pp. 16 335–16 362, Jun 2014.

[69] G. D. Forney, Jr. and L.-F. Wei, "Multidimensional constellations—part I: Introduction, figures of merit, and generalized cross constellations," *IEEE J. Sel. Areas Commun.*, vol. 7, no. 6, pp. 877–892, 1989.

[70] F. R. Kschischang and S. Pasupathy, "Optimal nonuniform signaling for Gaussian channels," *IEEE Trans. Inf. Theory*, vol. 39, no. 3, pp. 913–929, 1993.

[71] S. Benedetto and E. Biglieri, *Principles of Digital Transmission: With Wireless Applications*. New York, NY: Kluwer Academic, 1999.

[72] M. K. Simon and J. G. Smith, "Hexagonal multiple phase-and-amplitude-shift-keyed signal sets," *IEEE Trans. Commun.*, vol. 21, no. 10, pp. 1108–1115, 1973.

[73] J. G. Smith, "Odd-bit quadrature amplitude-shift keying," *IEEE Trans. Commun.*, vol. 23, no. 3, pp. 385–389, 1975.

[74] A. Alvarado, T. Fehenberger, B. Chen, and F. M. J. Willems, "Achievable information rates for fiber optics: Applications and computations," *J. Lightw. Technol.*, vol. 36, no. 2, pp. 424–439, 2018.

[75] G. Caire, G. Taricco, and E. Biglieri, "Bit-interleaved coded modulation," *IEEE Trans. Inf. Theory*, vol. 44, no. 3, pp. 927–946, 1998.

[76] E. Agrell and A. Alvarado, "Optimal alphabets and binary labelings for BICM at low SNR," *IEEE Trans. Inf. Theory*, vol. 57, no. 10, pp. 6650–6672, 2011.

[77] E. Agrell, M. Secondini, A. Alvarado, and T. Yoshida, "Performance prediction recipes for optical links," *IEEE Photon. Technol. Lett.*, vol. 33, no. 18, pp. 1034–1037, 2021.

[78] L. Schmalen, A. Alvarado, and R. Rios-Müller, "Performance prediction of nonbinary forward error correction in optical transmission experiments," *J. Lightw. Technol.*, vol. 35, no. 4, pp. 1015–1027, 2017.

[79] G. Liga, A. Alvarado, E. Agrell, and P. Bayvel, "Information rates of next-generation long-haul optical fiber systems using coded modulation," *J. Lightw. Technol.*, vol. 35, no. 1, pp. 113–123, 2017.

[80] A. Graell i Amat and L. Schmalen, "Forward error correction for optical transponders," in *Springer Handbook of Optical Networks*. B. Mukherjee, Ed. Cham, Switzerland: Springer, 2020, ch. 7.

[81] G. D. Forney, Jr., R. G. Gallager, G. R. Lang, F. M. Longstaff, and S. U. Qureshi, "Efficient modulation for band-limited channels," *IEEE J. Sel. Areas Commun.*, vol. 2, no. 5, pp. 632–647, 1984.

[82] L.-F. Wei, "Trellis-coded modulation with multidimensional constellations," *IEEE Trans. Inf. Theory*, vol. 33, no. 4, pp. 483–501, 1987.

[83] S. Zhang, F. Yaman, E. Mateo, T. Inoue, K. Nakamura, and Y. Inada, "Design and performance evaluation of a GMI-optimized 32QAM," in *Proc. Eur. Conf. Opt. Commun. (ECOC)*, Gothenburg, Sweden, Sept. 2017.

[84] R. T. Jones, T. A. Eriksson, M. P. Yankov, and D. Zibar, "Deep learning of geometric constellation shaping including fiber nonlinearities," in *Proc. Eur. Conf. Opt. Commun. (ECOC)*, Rome, Italy, Sept. 2018.

[85] S. Li, C. Häger, N. Garcia, and H. Wymeersch, "Achievable information rates for nonlinear fiber communication via end-to-end autoencoder learning," in *Proc. Eur. Conf. Opt. Commun. (ECOC)*, Rome, Italy, Sept. 2018.

[86] B. Chen, C. Okonkwo, H. Hafermann, and A. Alvarado, "Increasing achievable information rates via geometric shaping," in *Proc. Eur. Conf. Opt. Commun. (ECOC)*, Rome, Italy, Sept. 2018.

[87] K. Gümüş, A. Alvarado, B. Chen, C. Häger, and E. Agrell, "End-to-end learning of geometrical shaping maximizing generalized mutual information," in *Proc. Opt. Fiber Commun. Conf. (OFC)*, San Diego, CA, Mar. 2020.

[88] G. Rademacher, B. J. Puttnam, R. S. Luís, Y. Awaji, N. Wada, E. Agrell, and K. Petermann, "Experimental investigation of a 16-dimensional modulation format for long-haul multi-core fiber transmission," in *Proc. Eur. Conf. Opt. Commun. (ECOC)*, Valencia, Spain, 2015.

[89] D. S. Millar, T. Koike-Akino, K. Kojima, and K. Parsons, "A 24-dimensional modulation format achieving 6 dB asymptotic power efficiency," in *Proc. Sig. Proc. Photon. Commun. (SPPCom)*, Rio Grande, Puerto Rico, US, 2013, pp. SPM3D–6.

[90] T. Koike-Akino, D. S. Millar, K. Kojima, and K. Parsons, "Eight-dimensional modulation for coherent optical communications," in *Proc. Eur. Conf. Opt. Commun. (ECOC)*, London, UK, 2013.

[91] D. S. Millar, T. Koike-Akino, S. Ö. Arık, K. Kojima, K. Parsons, T. Yoshida, and T. Sugihara, "High-dimensional modulation for coherent optical communications systems," *Opt. Exp.*, vol. 22, no. 7, pp. 8798–8812, April 2014.

[92] S. Stern, M. Barakatain, F. Frey, J. K. Fischer, and R. F. H. Fischer, "Concatenated non-binary coding with 4D constellation shaping for high-throughput fiber-optic communication," in *Proc. Sig. Proc. Photon. Commun. (SPPCom)*, Washington, D.C., US, July 2021.

[93] S. Stern, M. Barakatain, F. Frey, J. Pfeiffer, J. K. Fischer, and R. F. H. Fischer, "Coded modulation for four-dimensional signal constellations with concatenated nonbinary forward error correction," in *Proc. Eur. Conf. Opt. Commun. (ECOC)*, Brussels, Belgium, Dec. 2020.

[94] E. Sillekens, G. Liga, D. Lavery, P. Bayvel, and R. I. Killey, "High-cardinality geometrical constellation shaping for the nonlinear fibre channel," *J. Lightw. Technol.*, vol. 40, no. 19, pp. 6374–6387, 2022.

[95] A. Mirani, E. Agrell, and M. Karlsson, "Low-complexity geometric shaping," *J. Lightw. Technol.*, vol. 39, no. 2, pp. 363–371, 2021.

[96] A. Mirani, K. Vijayan, Z. He, S. Li, E. Agrell, J. Schröder, P. Andrekson, and M. Karlsson, "Experimental demonstration of 8-dimensional Voronoi constellations with 65,536 and 16,777,216 symbols," in *Proc. Eur. Conf. Opt. Commun. (ECOC)*, Bordeaux, France, Sep. 2021.

[97] A. Mirani, K. Vijayan, S. Li, Z. He, J. Schröder, P. Andrekson, E. Agrell, and M. Karlsson, "Comparison of physical realizations of multidimensional Voronoi constellations in single mode fibers," in *Proc. Eur. Conf. Opt. Commun. (ECOC)*, Basel, Switzerland, Sept. 2022.

[98] A. Mirani, K. Vijayan, S. Li, Z. He, E. Agrell, J. Schröder, P. Andrekson, and M. Karlsson, "Physical realizations of multidimensional Voronoi constellations in optical communication systems," *J. Lightw. Technol.*, to appear, 2023.

[99] B. Chen, Z. Liang, S. Li, Y. Lei, G. Liga, and A. Alvarado, "On the performance of multidimensional constellation shaping for linear and nonlinear optical fiber channel," in *Proc. Eur. Conf. Opt. Commun. (ECOC)*, Glasgow, Scotland, Sept. 2023.

[100] T. Fehenberger, A. Alvarado, G. Böcherer, and N. Hanik, "On probabilistic shaping of quadrature amplitude modulation for the nonlinear fiber channel," *J. Lightw. Technol.*, vol. 34, no. 21, pp. 5063–5073, 2016.

[101] M. N. Tehrani, M. Torbatian, H. Sun, P. Mertz, and K.-T. Wu, "A novel nonlinearity tolerant super-Gaussian distribution for probabilistically shaped modulation," in *Proc. Eur. Conf. Opt. Commun. (ECOC)*, Rome, Italy, Sept. 2018.

[102] R. Dar, M. Feder, A. Mecozzi, and M. Shtaif, "On shaping gain in the nonlinear fiber-optic channel," in *Proc. IEEE Int. Symp. Inf. Theory (ISIT)*, June 2014, pp. 2794–2798.

[103] F.-W. Sun and H. C. A. van Tilborg, "Approaching capacity by equiprobable signaling on the Gaussian channel," *IEEE Trans. Inf. Theory*, vol. 39, no. 5, pp. 1714–1716, 1993.

[104] B. M. Oliveira, M. S. Neves, F. P. Guiomar, M. C. R. Medeiros, and P. P. Monteiro, "End-to-end deep learning of geometric shaping for unamplified coherent systems," *Optics Express*, vol. 30, no. 23, pp. 41 459–41 472, 2022.

[105] Z. Chen, Z. He, A. Mirani, J. Schröder, P. Andrekson, M. Karlsson, M. Xiang, Y. Yu, M. Tang, Y. Qin, and S. Fu, "Transmitter optimization for PS-QAM signal in high spectral efficiency metro-transmission," *J. Lightw. Technol.*, vol. 41, no. 9, pp. 2736–2746, 2023.

[106] A. Kakkavas, W. Xu, J. Luo, M. Castañeda, and J. A. Nossek, "On PAPR characteristics of DFT-s-OFDM with geometric and probabilistic constellation shaping," in *Proc. IEEE Intl. Workshop on Sig. Proc. Advances in Wireless Commun. (SPAWC)*, Sapporo, Japan, July 2017.

[107] G. D. Forney, Jr., *Concatenated codes*. Cambridge, MA: MIT Press, 1965.

[108] M. Barakatain, D. Lentner, G. Böecherer, and F. R. Kschischang, "Performance-complexity tradeoffs of concatenated FEC for higher-order modulation," *J. Lightw. Technol.*, vol. 38, no. 11, pp. 2944–2953, 2020.

[109] "Digital video broadcasting (DVB); Second generation framing structure, channel coding and modulation systems for broadcasting, interactive services, news gathering and other broadband satellite applications (DVBS2)," ETSI, Sophia Antipolis, France, Tech. Rep. ETSIEN 302 307 V1.2.1 (2009-08), Aug. 2009.

[110] H. Sun, M. Torbatian, M. Karimi, R. Maher, S. Thomson, M. Tehrani, Y. Gao, A. Kumpera, G. Soliman, A. Kakkar, M. Osman, Z. A. El-Sahn, C. Doggart, W. Hou, S. Sutarwala, Y. Wu, M. R. Chitgarha, V. Lal, H.-S. Tsai, S. Corzine, J. Zhang, J. Osenbach, S. Buggaveeti, Z. Morbi, M. I. Olmedo, I. Leung, X. Xu, P. Samra, V. Dominic, S. Sanders, M. Ziari, A. Napoli, B. Spinnler, K.-T. Wu, and P. Kandappan, "800G DSP ASIC design using probabilistic shaping and digital sub-carrier multiplexing," *J. Lightw. Technol.*, vol. 38, no. 17, pp. 4744–4756, 2020.

[111] S. B. Wicker and V. K. Bhargava, *Reed-Solomon codes and their applications*. John Wiley & Sons, 1999.

[112] G. D. Forney, Jr., "On decoding BCH codes," *IEEE Trans. Inf. Theory*, vol. 11, no. 4, pp. 549–557, 1965.

[113] B. P. Smith, A. Farhood, A. Hunt, F. R. Kschischang, and J. Lodge, "Staircase codes: FEC for 100 Gb/s OTN," *J. Lightw. Technol.*, vol. 30, no. 1, pp. 110–117, 2011.

[114] W. Wang, Z. Long, W. Qian, K. Tao, Z. Wei, S. Zhang, Z. Feng, Y. Xia, and Y. Chen, "Real-time FPGA investigation of potential FEC schemes for 800G-ZR/ZR+ forward error correction," *J. Lightw. Technol.*, vol. 41, no. 3, pp. 926–933, 2023.

[115] A. Y. Sukmadji, U. Martínez-Peñas, and F. R. Kschischang, "Zipper codes: Spatially-coupled product-like codes with iterative algebraic decoding," in *Proc. Can. Workshop on Inf. Theory (CWIT)*, 2019, pp. 1–6.

[116] G. Ungerboeck, "On improving data-link performance by increasing channel alphabet and introducing sequence coding," in *Proc. IEEE Int. Symp. Inf. Theory (ISIT)*, Ronneby, Sweden, June 1976.

[117] ——, "Channel coding with multilevel/phase signals," *IEEE Trans. Inf. Theory*, vol. 28, no. 1, pp. 55–67, 1982.

[118] A. J. Viterbi, "Error bounds for convolutional codes and an asymptotically optimum decoding algorithm," *IEEE Trans. Inf. Theory*, vol. 13, no. 2, pp. 260–269, 1967.

[119] G. Ungerboeck, "Trellis-coded modulation with redundant signal sets part I: Introduction," *IEEE Commun. Mag.*, vol. 25, no. 2, pp. 5–11, 1987.

[120] ——, "Trellis-coded modulation with redundant signal sets part II: State of the art," *IEEE Commun. Mag.*, vol. 25, no. 2, pp. 12–21, 1987.

[121] H. Imai and S. Hirakawa, "A new multilevel coding method using error-correcting codes," *IEEE Trans. Inf. Theory*, vol. 23, no. 3, pp. 371–377, 1977.

[122] U. Wachsmann, R. F. H. Fischer, and J. B. Huber, "Multilevel codes: theoretical concepts and practical design rules," *IEEE Trans. Inf. Theory*, vol. 45, no. 5, pp. 1361–1391, 1999.

[123] A. Alvarado, F. Brännström, E. Agrell, and T. Koch, "High-SNR asymptotics of mutual information for discrete constellations with applications to BICM," *IEEE Trans. Inf. Theory*, vol. 60, no. 2, pp. 1061–1076, 2014.

[124] A. J. Viterbi, "An intuitive justification and a simplified implementation of the MAP decoder for convolutional codes," *IEEE J. Sel. Areas Commun.*, vol. 16, no. 2, pp. 260–264, 1998.

[125] J. H. Conway and N. J. A. Sloane, *Sphere Packings, Lattices and Groups*, 3rd ed. New York, NY: Springer, 1999.

[126] D. Pook-Kolb, E. Agrell, and B. Allen, "The Voronoi region of the Barnes–Wall Lattice Λ_{16}," *IEEE J. Sel. Areas Commun.*, Early Access, 2023, doi: 10.1109/JSAIT.2023.3276897.

[127] N. J. A. Sloane, "Tables of sphere packings and spherical codes," *IEEE Trans. Inf. Theory*, vol. 27, no. 3, pp. 327–338, 1981.

[128] J. H. Conway and N. J. A. Sloane, "On the Voronoi regions of certain lattices," *SIAM J. Alg. Disc. Meth.*, vol. 5, no. 3, pp. 294–305, 1984.

[129] C. Feng, D. Silva, and F. R. Kschischang, "An algebraic approach to physical-layer network coding," *IEEE Trans. Inf. Theory*, vol. 59, no. 11, pp. 7576–7596, 2013.

[130] W. C. Brown, *Matrices over Commutative Rings*. New York, NY: Marcel Dekker, 1993.

[131] N. S. Ferdinand, B. M. Kurkoski, B. Aazhang, and M. Latva-aho, "Shaping low-density lattice codes using Voronoi integers," in *Proc. IEEE Inf. Theory Workshop (ITW)*, Hobart, Australia, Nov. 2014.

[132] M. Isaka, R. H. Morelos-Zaragoza, M. P. C. Fossorier, S. Lin, and H. Imai, "Multilevel coded 16-QAM modulation with multistage decoding and unequal error protection," in *Proc. IEEE Glob. Commun. Conf. (GLOBECOM)*, Sydney, NSW, Australia, 1998, pp. 3548–3553.

[133] R. Yuan, J. Fang, R. Xu, B. Bai, and J. Wang, "A hybrid MLC and BICM coded-modulation framework for 6G," in *Proc. IEEE Globecom Workshops (GC Wkshps)*, Madrid, Spain, 2021.

[134] L. Beygi, E. Agrell, J. M. Kahn, and M. Karlsson, "Rate-adaptive coded modulation for fiber-optic communications," *J. Lightw. Technol.*, vol. 32, no. 2, pp. 333–343, 2014.

[135] F. Frey, S. Stern, J. K. Fischer, and R. F. H. Fischer, "Two-stage coded modulation for Hurwitz constellations in fiber-optical communications," *J. Lightw. Technol.*, vol. 38, no. 12, pp. 3135–3146, 2020.

[136] A. R. Calderbank and N. J. A. Sloane, "New trellis codes based on lattices and cosets," *IEEE Trans. Inf. Theory*, vol. 33, no. 2, pp. 177–195, 1987.

[137] G. D. Forney, Jr., "Coset codes—part I: Introduction and geometrical classification," *IEEE Trans. Inf. Theory*, vol. 34, no. 5, pp. 1123–1151, 1988.

[138] A. B. Owen, "Monte Carlo theory, methods and examples," 2013. [Online]. Available: https://statweb.stanford.edu/~owen/mc

[139] H. Kahn and A. W. Marshall, "Methods of reducing sample size in Monte Carlo computations," *Am. J. Oper. Res. Soc.*, vol. 1, no. 5, pp. 263–278, 1953.